Title: Electrode position, size, and orientation determine efficacy of cervical epidural stimulation to recruit forelimb muscles in rats

Andrés Pascual-Leone[1,2*], Vishweshwar Tyagi[2*], Ahmet S. Asan[2*], Pedro Emanuel Rocha-Flores[3], Ovidio Rodriguez-Lopez[4], Walter Voit[5], James R. McIntosh[2**], Jason B. Carmel[2**†]

[1]Dept. of Neurological Surgery, Columbia University, New York, NY, USA.

[2]Dept. of Neurology, Columbia University, New York, NY, USA.

[3]Dept. of Biomedical Engineering, University of Texas at Dallas, Richardson, TX, USA

[4]Center for Engineering Innovation, University of Texas at Dallas, Richardson, TX, USA

[5]Dept. of Materials Science and Engineering, University of Texas at Dallas, Richardson, TX, USA

* = These authors contributed equally to this work

** = Senior authors contributed equally and share senior authorship

†Corresponding author: Dr. Jason B. Carmel, jbc28@cumc.columbia.edu

Abstract

Objective

Cervical epidural spinal cord stimulation (SCS) can facilitate upper-limb motor recovery, but electrode configurations that optimally recruit motor circuits remain unclear. This study systematically evaluated how electrode position, size, orientation, and waveform influence the efficacy of forelimb motor activation in rats, with the goal of identifying configurations that minimize stimulation thresholds of evoked responses across multiple muscles.

Approach

Custom microfabricated arrays of electrodes were implanted over the C6 dorsal root entry zone (DREZ) in eight adult female Sprague Dawley rats. A circular array was used to vary current orientation in 45° increments, while a linear array was used to optimize mediolateral electrode position. The linear array included both small (250 µm) and large (500 µm) contacts to assess size effects at mediolateral positions. Stimulation consisted of biphasic and pseudomonophasic waveforms with bipolar or distant return, and a high-definition montage to probe spatial focality around the DREZ. Motor-evoked potentials (MEPs) recorded via implanted EMG electrodes were analyzed in six forelimb muscles. Thresholds, estimated from recruitment curves using a hierarchical Bayesian model, were compared within-rat using pairwise t-tests with correction for multiple comparisons.

Results

Stimulation over the DREZ yielded the lowest thresholds and efficacy decreased progressively with medial or lateral displacement relative to DREZ. In the circular array, rostro-caudal current orientation was most effective, reducing thresholds by up to 58% relative to latero-medial orientation ($p = 0.0007$). In the linear array, large contacts were significantly more effective than small contacts at the lateral position, reducing thresholds by 45% ($p = 0.034$). Cathodal stimulation was more effective than anodal, and high-definition montages reduced efficacy compared to distant returns. Across all tested parameters, position and orientation had the greatest influence on efficacy, with optimal conditions combining DREZ targeting and rostro-caudal oriented current flow.

Significance

Maximum efficacy was achieved for cervical SCS with electrodes positioned over the DREZ, rostro-caudal current flow, larger contacts, and cathodal stimulation. These design principles that more effectively engage spinal circuitry could reduce the current required and thereby improve SCS systems for upper-limb motor restoration.

1 Introduction

Target engagement and selectivity determine therapeutic efficacy. In neuromodulation, these attributes are shaped by the arrangement of electrodes and electrical stimulation parameters. Although spinal cord stimulation (SCS) is widely employed in research and clinical care, many stimulation parameters remain unexplored. In this study, we aimed to systematically evaluate epidural stimulation configurations using hypothesis-driven, custom-built arrays of electrodes. Our goal was to identify stimulation strategies that most effectively evoke motor responses and thereby optimally engage the spinal circuits that control forelimb movement.

Both animal and computational models of SCS indicate that dorsal epidural stimulation at low intensities primarily recruits large diameter afferent fibers (Capogrosso et al. 2013; Rattay et al. 2000; Greiner et al. 2021). These afferents synapse both directly and indirectly onto motoneurons; when stimulated at higher intensities, these generate motor responses (Renshaw 1940; Lloyd 1943). The resultant effect of afferent activation can be objectively quantified using electromyography (EMG). In the context of movement recovery, an important application of SCS, EMG provides the ability to directly observe a physiological response to stimulation, the motor evoked potential (MEP). Our previous studies have shown a strong concordance between stimuli that produce strong MEPs and those that promote adaptive plasticity (Yang et al. 2019; Pal et al. 2022). Experimental protocols can therefore be designed to systematically compare stimulation parameters and optimize therapeutic efficacy using MEP threshold as the main outcome measure. For functional recovery, electrode configurations and current patterns that most effectively engage large diameter afferents are likely to produce MEPs at low stimulation intensity.

SCS electrode position plays a crucial role in the muscles that are recruited. Our group and others have demonstrated that when keeping spinal level constant, lateral epidural stimulation is more effective than medial stimulation in the rat, and the most effective electrode position is over the dorsal root entry zone (DREZ) (Mishra et al. 2017; Wenger et al. 2016). Similarly, in human intraoperative mapping experiments, our group showed epidural stimulation over the DREZ generates larger MEPs than midline stimulation in the cervical spinal cord (McIntosh et al. 2023). In addition to the proximity of the electrodes to the dorsal root in this position, the sharp change in angle of the afferent fibers as they enter the spinal cord may explain the enhanced stimulation efficacy observed near the DREZ (Rattay et al. 2014). Using arrays that examined multiple degrees of laterality relative to midline, we hypothesized that stimulation centered at the DREZ would be optimal, with loss of SCS effectiveness as the site of stimulation moved lateral or medial to the DREZ.

Modeling studies have demonstrated an impact of contact size on neural activation efficacy (Holsheimer et al. 1995; Zander et al. 2022). In clinical SCS studies for chronic pain, larger paddle lead devices allowed

for lower amplitudes with longer sustained pain relief compared to smaller percutaneous contacts (North et al. 2002; 2005). Similarly, in animal models, larger contacts activated target motor neurons more effectively than small contacts, while very small (100-200 µm) contacts in densely packed configurations might enable higher selectivity (Mao et al. 2022; Russman et al. 2025). This suggests contact size might be an important variable of effective stimulation.

Stimulation waveform and electrical current direction also determine the efficacy of SCS. Contrary to stimulation in the cortex, monopolar cathodal stimulation is more effective than anodal stimulation for epidural spinal stimulation (Struijk et al. 1993; Coburn 1985; Alam et al. 2015). Alam et al. reported that monophasic bipolar stimulation across segments is superior to monopolar stimulation at a single segment for eliciting MEPs and subsequently showed that bipolar stimulation enhanced forelimb recovery after a C4 spinal cord injury in rats (Alam et al. 2015; 2017). Furthermore, computational models have demonstrated the importance of cathode positioning relative to the spinal cord (Ladenbauer et al. 2010; Zander et al. 2020). Cuellar et al. used a 4-contact array to stimulate at 45-degree radial increments, however an optimum orientation could not be identified (Cuellar et al. 2024). Computational models have shown that activation of nerve fibers by external stimulation is governed by changes in the electrical potential along the fiber (Rattay 1986; Ladenbauer et al. 2010). Therefore, we predict that aligning the current with the entering nerve roots would elicit the largest responses.

Precise testing of electrode position, size, and orientation has been limited by a lack of technology to precisely pattern electrodes. For example, the 4-contact array used by Cuellar et al. meant that combined activation of three contacts was required to select 45-degree increments of electrical current orientation, which is likely to have complex current spread. We and others have used photolithography to enable printing of electrodes of any size or position (Rocha-Flores et al. 2025; Garcia-Sandoval et al. 2018; Rocha-Flores et al. 2023; Meacham et al. 2008; Nandra et al. 2011; Minev et al. 2015). We used a softening polymer that creates a tight neural interface with the underlying dura. We patterned these devices with electrodes specifically designed to test electrode position, size, and orientation. We also tested different waveforms including a high-definition montage that has been shown to increase spatial focality for brain stimulation (Datta et al. 2008; 2009). Across conditions, differences in efficacy were defined as the ratio of thresholds for provoking a MEP using a recruitment curve. We have previously demonstrated that analysis of recruitment curves allows accurate estimates of motor thresholds across multiple muscles (Tyagi et al. 2024). We used the custom electrodes, automated and randomized stimulation, and recruitment curve analysis to determine the effects of different electrode patterns and stimulation waveforms.

2 Methods

2.1 Summary

We stimulated the cervical spinal cord of 8 rats using different electrode configurations and polarities while recording muscle responses. The effects of electrode position, orientation, size and stimulation polarity were compared using the threshold for creating a motor evoked potential (MEP). The experimental setup is shown in Fig. 1. In Fig. 1A, the target muscles for electromyogram (EMG) are depicted. These were chosen to represent each of the segments of the cervical enlargement. The electrodes were printed onto arrays using photolithography, which enables them to be patterned to help answer questions about how best to stimulate the cervical spinal cord. Fig. 1B shows the two devices with the circular device on the left and the linear device on the right. Fig. 1C shows a computerized rendering of how the SCS device is implanted through a C4 laminectomy. The substrate of the SCS device is a softening polymer; once placed on the spinal cord, the softening polymer allows the array to conform to the curvature of the underlying dura. In Fig. 1D, the three electrode configurations are shown: 1. circular electrodes with the central electrode over the dorsal root entry zone, 2. small linear electrodes, and 3. large linear electrodes. It is important to emphasize that the electrodes were targeted to the same segment–the linear electrodes were repositioned between testing of the small and large electrodes so that they were in the same rostro-caudal location for each comparison. Fig. 1E shows the relative positions of the circular and linear arrays overlaid on one another.

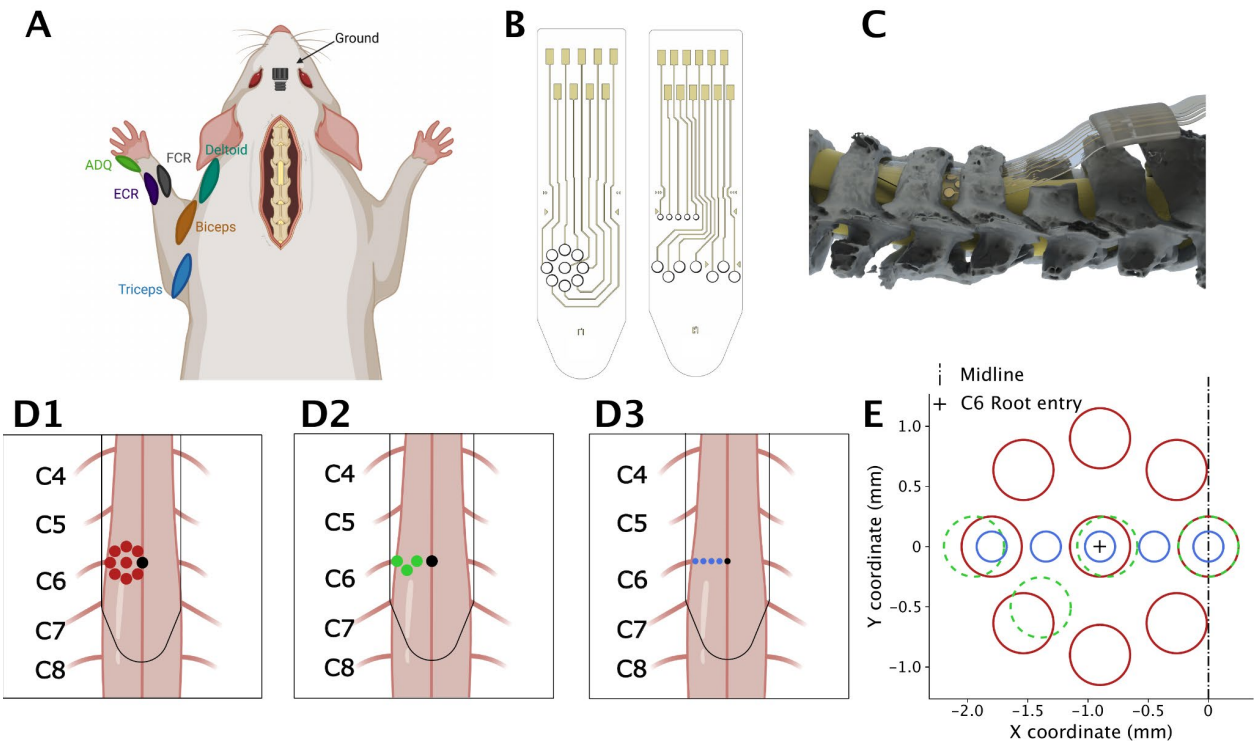

Figure 1. Experimental setup. (A) EMG electrodes were implanted in muscles of the rat's left forelimb. A ground electrode was placed at the skull midline, over the olfactory bulbs and between the eyes. FCR-Flexor carpi radialis. ECR-extensor carpi radialis. ADQ-abductor digiti quinti. Created in BioRender. Pascual-Leone, A. (2025) https://BioRender.com/18tnpip **(B)** Circular array (left) and linear array (right, with big and small contacts) were designed to test effects of orientation, position, and contact size on stimulation efficacy. **(C)** Computer rendering based on micro-CT showing epidural insertion of an electrode following a C4 laminectomy. The electrode, fabricated from a softening polymer, conforms to the spinal cord curvature. **(D)** Electrodes were placed epidurally on the dorsal surface of the spinal cord, targeting the dorsal root entry zone (DREZ) at the C6 segment. For the linear array, the electrode was repositioned between trials to allow both large and small contacts to be tested at the same spinal level. Black circles mark midline contact positions. Due to the design of this array, we additionally tested the C5 segment in these experiments. D1: circular array; D2: large-contact linear array; D3: small-contact linear array. **(E)** Schematic overview of the spatial overlap across the three electrode arrays, showing their relative alignment.

2.2 Spinal cord electrode array design and microfabrication

Electrode design began with the careful dissection and measurement of the spinal cords of three rats. The spinal cords were photographed under a microscope and the location of the DREZ was digitally annotated. Each spinal cord was then transformed into a common grid space relative to the C6 midline and the three cords were overlaid to determine the average coordinates of the DREZ on an X-Y plane. Following the creation of an averaged spinal cord, we designed two custom arrays to test specific hypotheses of spinal cord stimulation (Fig. 1B). To test the importance of current flow orientation relative to DREZ and the

efficacy of a high-definition configuration, we designed the circular array such that the central contact was directly over the C6 DREZ and surrounded with electrodes in a circle around this central electrode. To test the importance of mediolateral position, the linear arrays were designed to enable stimulation at multiple locations, with an electrode centered over the DREZ being common to all three arrays. The size of the small linear electrodes (250 µm in diameter) and large linear electrodes (500 µm) were chosen based on previous experiments and to approximate the electrode to spinal cord dimension ratios of human devices.

The fabrication of the spinal cord devices was conducted in a cleanroom facility using a softening polymer and standard microfabrication methods which have previously been described (Garcia-Sandoval et al. 2018; Rocha-Flores et al. 2023). The microfabrication process began with a 50 µm polymer layer coated on a glass wafer to make it compatible with typical silicon processes. Subsequently, a 300 nm layer of gold was deposited on top of the softening polymer using e-beam evaporation. An adhesion layer of titanium with a thickness of 30 nm, deposited under a 100% Argon atmosphere using radio frequency sputtering, separated the gold and titanium nitride layers. A 240 nm thick layer of titanium nitride was then deposited in an argon:nitrogen mixture with a ratio of 19:1 to serve as a coating material for the electrodes under the same vacuum conditions. The lithography process and wet etch process were employed to define the electrode positions and gold metal traces, utilizing 22:7 nitric acid and hydrofluoric acid for the wet etching process and a potassium iodide solution in a 2:1 ratio with water for the development of the pattern. Subsequently, a second 50 µm polymer layer was spin-coated to act as an encapsulation layer. A layer of silicon nitride was deposited using plasma-enhanced chemical vapor deposition to protect the polymer during a selective etching process carried out in a reactive-ion etching system, using an oxygen atmosphere to pattern the device outlines and to create openings to the electrodes and the connecting pads. Following the dry etching process, hydrofluoric acid (HF) was used for any remaining hard mask. The glass wafers were submerged in deionized water for 18 hours to release the devices. Finally, after the release process, the devices were subjected to typical electrochemical characterization techniques, including cyclic voltammetry, electrochemical impedance spectroscopy, and voltage transient analysis to ensure functionality and device quality.

2.3 Surgical procedures

2.3.1 Rats

Eight adult female Sprague Dawley rats were used in this study for a terminal physiology experiment. All procedures were conducted in compliance with the guidelines of the Institutional Animal Care and Use Committee at Columbia University in New York, NY, and followed aseptic techniques. Experiments were performed under anesthesia to enable testing with different devices. The rats were initially anesthetized with a mixture of ketamine (90 mg/kg) and xylazine (10 mg/kg). Anesthesia levels were subsequently

maintained using supplemental injection of ketamine at one-third of the initial dosage, administered as needed based on the continual assessment of the hindlimb pinch reflex. Following the initial anesthesia, the animals were placed in a stereotaxic frame with their heads fixed. Body temperature was maintained at 37.5 degrees during the procedure, with continuous monitoring using a rectal probe and heat delivered as needed by a warming pad. Blood oxygen levels were monitored with a pulse oximeter. Hair was removed from the top of the head, along the back, and over the right and left forelimbs. The skin was then cleaned with alcohol and an antiseptic solution. A midline incision was made, extending from between the eyes to the T1 vertebra. Connective tissue covering the skull was excised, and the muscles were separated to access the cervical spine. A hole was drilled into the skull over the olfactory bulbs and a screw electrode was inserted into the hole as a ground electrode.

2.3.2 EMG implant

EMG was recorded from eight different muscles: left extensor carpi radialis (ECR), flexor carpi radialis (FCR), biceps, triceps, abductor digiti quinti (ADQ), deltoid, biceps femoris, and right biceps. Flexible, braided stainless steel wires (106.1 um, AS634, A-M system; Washington, USA) were employed for EMG recording. These electrodes were soldered to the connector and covered with epoxy to ensure insulation. Subsequently, the connector was attached to the recording system. Wire insulation was removed for 1 mm, starting from 2 cm away from the tip, corresponding to the muscle belly. A twenty-gauge needle was inserted into the muscles, and the wires were passed through the needle, allowing their tips to emerge on the opposite side of the muscle. The needle was then gently withdrawn while leaving the wire inside the muscle. Once the uninsulated part of the wire was positioned within the muscle belly, the wire tip was securely knotted and adhered to the muscle using gluture topical adhesive (World Precision Instruments; Florida, USA) to prevent potential movement. If necessary, the muscle was covered with skin and sutured to prevent it from drying out.

2.3.3 Spinal cord electrode placement

After placing the EMG electrodes, the muscles over the spinal cord were separated, and the T1 spinous process was clamped to stabilize the spine. A laminectomy was performed to bilaterally expose the C4 cervical spinal cord. Arrays were then carefully inserted into the dorsal epidural space over the cervical enlargement (C5-C8). We used bony and anatomical landmarks to identify the root entry zone. The intervertebral foramen also provided an opening for visual confirmation of the target site. Omnetics (Omnetics Connector Corp.; Minnesota, USA) connectors for the spinal array were attached to the stimulation system. Electrode impedance was checked both *in vitro* and *in vivo* before and after placement to ensure their quality. As various SCS arrays were used in this study (Fig. 1D), they were replaced sequentially, starting with the large electrode, followed by the circular, and then the small electrode.

When using the circular electrode configuration, the center contact was placed over the C6 dorsal root entry zone. When using the linear electrode configuration, the array was segmentally advanced to individually target with both large and small contact rows each DREZ at C5 and C6. Thus, both contact sizes stimulated both levels.

2.4 Electrophysiology and stimulation

Connectors for the spinal cord array and EMG wires were attached to a headstage ZIF-connector (Tucker-Davis Technologies; Florida, USA). The headstage connectors were used to interface the implanted electrodes with an amplifier (Tucker-Davis Technologies, PZ5), which was then connected to a real-time signal processing system (RZ2). A 16-channel IZ2H/Subject Interface constant current stimulator (Tucker-Davis Technologies) was controlled via a custom Matlab (R2022a) codebase. Single-pulse stimulation was delivered with various pulse shapes (biphasic and pseudomonophasic, Fig. 7) with equal pulse widths of 200 µs in their leading phase every 2 seconds. A charge balancing period of 800 µs was used for pseudomonophasic pulses. In order to determine the maximum stimulation intensity for each rat and device, we manually increased intensity while monitoring the animal. The maximum was defined as the lowest intensity that first evoked visible trunk movement. To generate recruitment curves, stimulation intensities were subsequently linearly increased from 0 to the maximum intensity (350 ± 207 µA) across 51 steps. This resulted in a step size of 6.43 ± 3.4 µA. Stimulation patterns were randomly applied across all combinations of contacts for an individual array, excluding high impedance contacts from testing. EMG signals were sampled at 10kHz and high-pass filtered using a 20 Hz cutoff 10th order IIR filter. A total of 135,018 MEPs across all rats and stimulation experiments were quantified from biceps, triceps, ECR, FCR, APB and ADQ ipsilateral to the side of stimulation. Contralateral biceps and biceps femoris were excluded from subsequent analyses as we were primarily interested in ipsilateral forelimb activation. Further explanation of the quantification is in section 2.5 and 2.6.

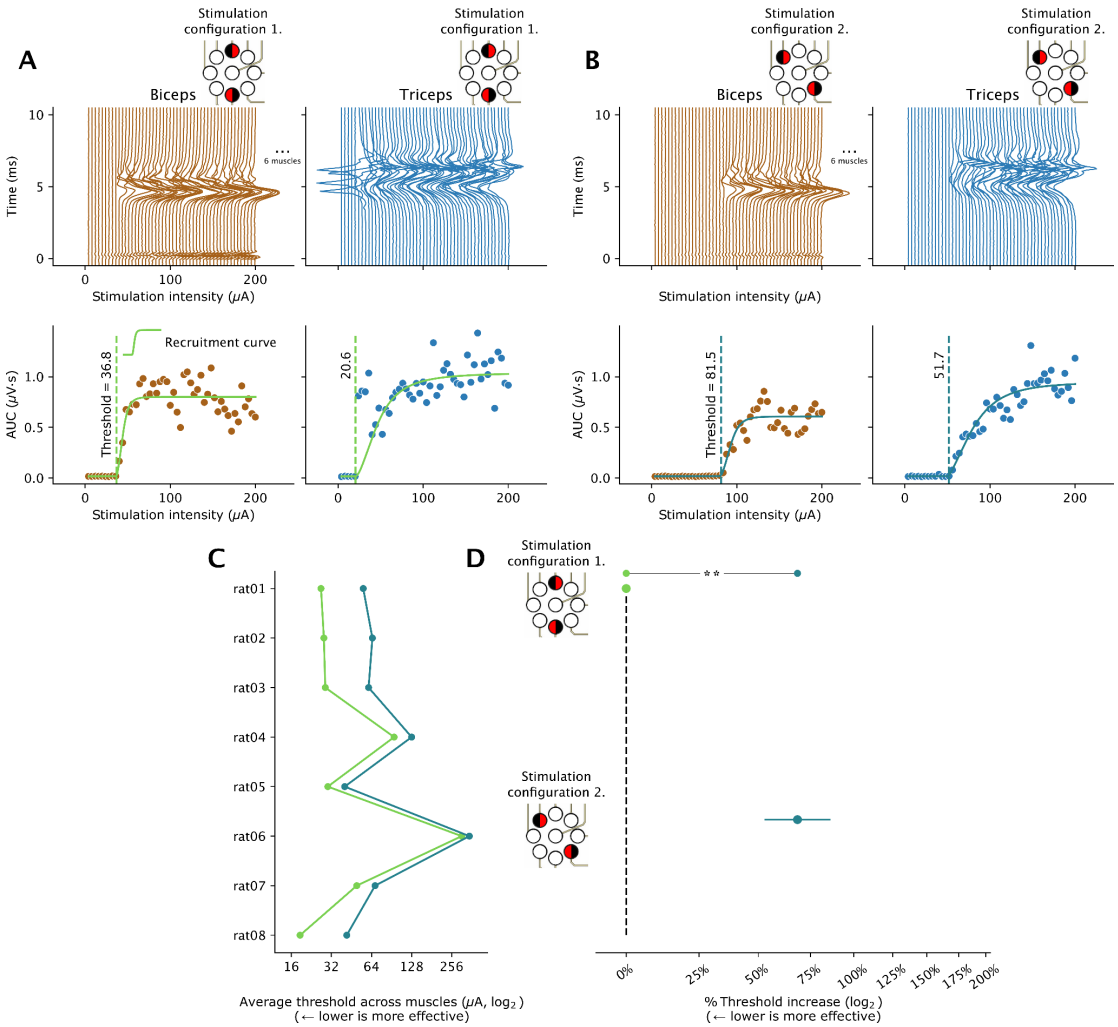

Figure 2. Estimation of recruitment curves and efficacy analysis. (A) Example motor-evoked potentials (MEPs) recorded from multiple muscles of a rat following stimulation with a circular electrode in the rostro-caudal orientation. Biphasic stimulation is represented by dual shaded contacts with red-black denoting an anode-cathode sequence and black-red a cathode-anode sequence at that particular contact. Bottom panels: MEPs are quantified by their area under the curve (AUC), and recruitment curves (solid curve) are fit, which yield threshold estimates (vertical dashed line). **(B)** Same as (A), but for the root-perpendicular orientation. It results in higher thresholds compared to rostro-caudal. **(C)** Thresholds averaged across six tested muscles are shown for each rat on a $\log_2$ scale. Dot and line colors correspond to different stimulation conditions (e.g. configuration in A is green and configuration B is blue). Lighter shades of green indicate configurations that yield lower thresholds and are therefore more effective at activating muscles. **(D)** Pairwise within-rat differences on a $\log_2$ scale, expressed as the percentage increase in threshold relative to the most effective configuration (configuration 1). Dots represent mean differences across rats, and error bars represent the standard error of the mean. As the reference, configuration 1 has no error bars. Asterisks with connecting lines indicate statistically significant differences between conditions, annotated as *p*-values: $p < 0.05$*, $p < 0.01$**, $p < 0.001$***.

2.5 Outcome measure

We defined efficacy as the average threshold across tested muscles, as our outcome measure. Thresholds were estimated simultaneously for all six tested muscles from recruitment curves (as explained below) and defined as the stimulation intensity required to evoke minimal consistent MEPs (Tyagi et al. 2024). Stimulation configurations yielding lower thresholds were considered more effective, as they facilitated muscle activation more readily. In addition to being a standard measure of spinal excitability (Pal et al. 2022), threshold was chosen because it likely reflects afferent activation. In contrast, MEP amplitudes at higher stimulation intensities may reflect mixed afferent and efferent contributions (Sharma and Shah 2021; Wecht et al. 2021).

2.6 Estimation of recruitment curves and efficacy analysis

We fit recruitment curves to MEP size data for each muscle to estimate thresholds. Let $a^{r,c,m}$ denote the threshold for rat r, muscle m, and stimulation configuration c. We model thresholds on the $\log_2$ scale to assess multiplicative changes between stimulation configurations. On this scale, a one unit change represents a two-fold change on the original scale. We define the rat-level average threshold $\log a^{r,c}$ to be the arithmetic mean of log-transformed thresholds $\log a^{r,c,m}$ across the six tested muscles (Eq. 2.1), which is equivalent to the log of their geometric mean (Eq. 2.2). In the case of the linear array, which was tested at two cervical segments (C5 and C6), we additionally averaged thresholds across segments.

$$\log a^{r,c} = \frac{1}{M}\sum_{m=1}^{M} \log a^{r,c,m} \tag{2.1}$$

$$= \log\left[\left(\prod_{m=1}^{M} a^{r,c,m}\right)^{\frac{1}{M}}\right] \tag{2.2}$$

To compare stimulation configurations c_1 and c_2, we define the within-rat difference Δ^{r,c_1,c_2} as the change in average threshold (Eq. 2.3), which is equivalent to the log geometric mean of their paired threshold ratios (Eq. 2.4) and provides a direct assessment of multiplicative changes between the thresholds of c_1 and c_2.

$$\Delta^{r,c_1,c_2} = \log a^{r,c_1} - \log a^{r,c_2} \tag{2.3}$$

$$= \log\left[\left(\prod_{m=1}^{M} \frac{a^{r,c_1,m}}{a^{r,c_2,m}}\right)^{\frac{1}{M}}\right] \tag{2.4}$$

The log-transformed muscle-level thresholds $\log a^{r,c,m}$ were estimated directly from recruitment curves using hbMEP (Tyagi et al. 2024). Fig. 2A,B show example MEPs recorded simultaneously from multiple muscles (upper panels), quantified by their area under the curve (AUC, lower panels). The resulting MEP size measurements were regressed against log-transformed stimulation intensity to estimate recruitment curves. Fig. 2A,B (lower panels) show the resulting curves, displayed on the original stimulation intensity scale (µA). We used a standard hierarchical Bayesian model from hbMEP to estimate curves as a rectified-logistic function (Tyagi et al. 2024). We used a mixture extension of the model to handle outliers without discarding any data. This model yielded posterior distributions of curve parameters, including threshold, and the median posterior value was used as point threshold estimate (Fig. 2A,B lower panels, vertical dashed line) for subsequent efficacy analysis.

To assess statistically significant differences in efficacy of configurations c_1 and c_2, we tested whether the mean difference across rats ($\mu_{\Delta}^{c_1,c_2}$) differed from zero using a two-sided one-sample t-test. This is equivalent to testing whether the geometric mean of paired threshold ratios deviated from one (Eq. 2.4). A positive difference indicated that configuration c_2 yielded lower thresholds and was thus more effective. Fig. 2 reports threshold differences as mean ± standard error of the mean (SEM) on the log scale and *p*-values are reported after correcting for multiple comparisons (see Methods 2.8 Statistics & reproducibility).

In cases where certain configurations were tested on fewer rats, for example, due to high impedance with large contacts, the frequentist t-test was underpowered to detect differences. For these cases, we used Bayesian estimation to compare efficacy within a hierarchical Bayesian framework (Tyagi et al. 2024). Instead of point threshold estimates, this approach utilizes their full posterior distribution and propagates posterior uncertainty to compute the distribution of threshold differences between configurations. When the difference posterior for one configuration lays predominantly to the left of the other with low overlap, it indicates a high probability of lower thresholds and therefore greater efficacy.

2.7 Selectivity analysis

Selectivity was quantified using the area under the recruitment curve, which quantifies the total motor evoked output in the interval of integration. Estimation of recruitment curves yielded estimates for two additional curve parameters, the offset L (representing baseline noise) and the saturation distance H (distance from offset to maximum response). To isolate the evoked response, curves were baseline-corrected by subtracting the offset $L = 0$, making H the effective saturating MEP size. Curves were then normalized for each rat r and muscle m by the maximum saturation across all tested stimulation configurations $H_{\max}^{r,m} = \max_{c} H^{r,c,m}$. This yielded normalized recruitment curves bounded between 0 and 1.

Muscle-level selectivity was defined as $S^{r,c,m} = A^{r,c,m} - \frac{1}{M-1} \sum_{m' \neq m} A^{r,c,m'}$ where M is the number of muscles (in our case, $M = 6$) and $A^{r,c,m}$ represents the area under normalized recruitment curve computed in the interval $\left[\min_m a^{r,c,m},\ \min_m a^{r,c,m} + 1\right]$. On the original intensity scale, this corresponds to integrating from the lowest muscle-level threshold to twice that threshold, thereby focusing on the early rising phase of muscle recruitment. This differs from previous approaches that integrated over the entire stimulation range (Bryson et al., 2023) or used maximum normalized amplitude differences (Greiner et al., 2021).

To summarize selectivity at the configuration level, we took the maximum muscle selectivity $S^{r,c} = \max_m S^{r,c,m}$, which quantifies how strongly any single muscle is isolated relative to all others.

Pairwise comparisons of configuration-level selectivity were performed using within-rat paired t-tests, following the same procedure as given in the efficacy analysis (Methods 2.6).

2.8 Statistics & reproducibility

All recruitment curves were fitted using hbMEP (Tyagi et al. 2024) and median posterior values were used as point threshold estimates. Threshold differences between stimulation configurations are reported as mean difference across rats ± standard error of the mean (SEM) on the log (base 2) scale, and expressed as percentage threshold increase relative to the most effective configuration. All p-values are reported after correcting for multiple comparisons and significance levels are annotated as $p < 0.05$*, $p < 0.01$**, and $p < 0.001$***.

For an analysis involving n stimulation configurations, all $\binom{n}{2}$ pairwise comparisons were conducted using one-sample t-tests, and resulting p-values were corrected for multiple comparisons using the Benjamini-Hochberg false discovery rate (FDR) procedure (Benjamini and Hochberg 1995), implemented using SciPy (Virtanen et al. 2020). For the size comparison, which involved comparing large and small electrodes at four different mediolateral positions (i.e. the same comparison repeated four times), a Bonferroni-Holm correction was applied to control the family-wise error rate.

The code to reproduce the presented analyses is available on GitHub (see 5.1.5 Code availability 5.6).

3 Results

3.1 Position: Stimulation over DREZ is most effective

We stimulated at multiple mediolateral positions in both linear and circular arrays with a distant return.

On the linear array, four positions were available for both large and small contacts: midline (M), lateromedial (LM), lateral (L), and far lateral (LL) (Fig. 3). The small-contact configuration additionally included a second lateromedial position (LM2). Each contact size was analyzed separately to assess the effect of mediolateral position, with LM being the contact that optimally aligned over the DREZ for both sizes.

For small contacts, LM was the most effective, and yielded the lowest thresholds (Fig. 3A, Supplementary Fig. S1A). Relative to LM, thresholds were significantly higher for LL (80%, 0.846 ± 0.234, $p = 0.029$), M (51%, 0.595 ± 0.179, $p = 0.029$), and L (31%, 0.388 ± 0.118, $p = 0.029$), while LM2 was only slightly higher (10%, 0.144 ± 0.063, $p = 0.08$). Relative to LM2, thresholds were also significantly higher for LL (63%, 0.703 ± 0.218, $p = 0.029$) and M (37%, 0.452 ± 0.162, $p = 0.045$). Overall, efficacy ranked from highest to lowest as: LM, LM2, L, M, and LL, with efficacy decreasing as the electrode position moved further away from the DREZ at LM. See Supplementary Fig. S1A for all pairwise comparisons.

For large contacts, high impedance (possibly air under the stimulating electrode) limited the number of rats tested in some lateral positions, reducing the power to detect differences. Despite this, the overall efficacy ranking was similar to that observed with small contacts, with LM being most effective (Fig. 3B, Supplementary Fig. S1B). Given the small sample size, we compared the efficacy of large contacts using Bayesian estimation (Tyagi et al. 2024), which indicated that LM and L were equally effective and both significantly more effective than M and LL, with M yielding lower thresholds that LL (Supplementary Fig. S2).

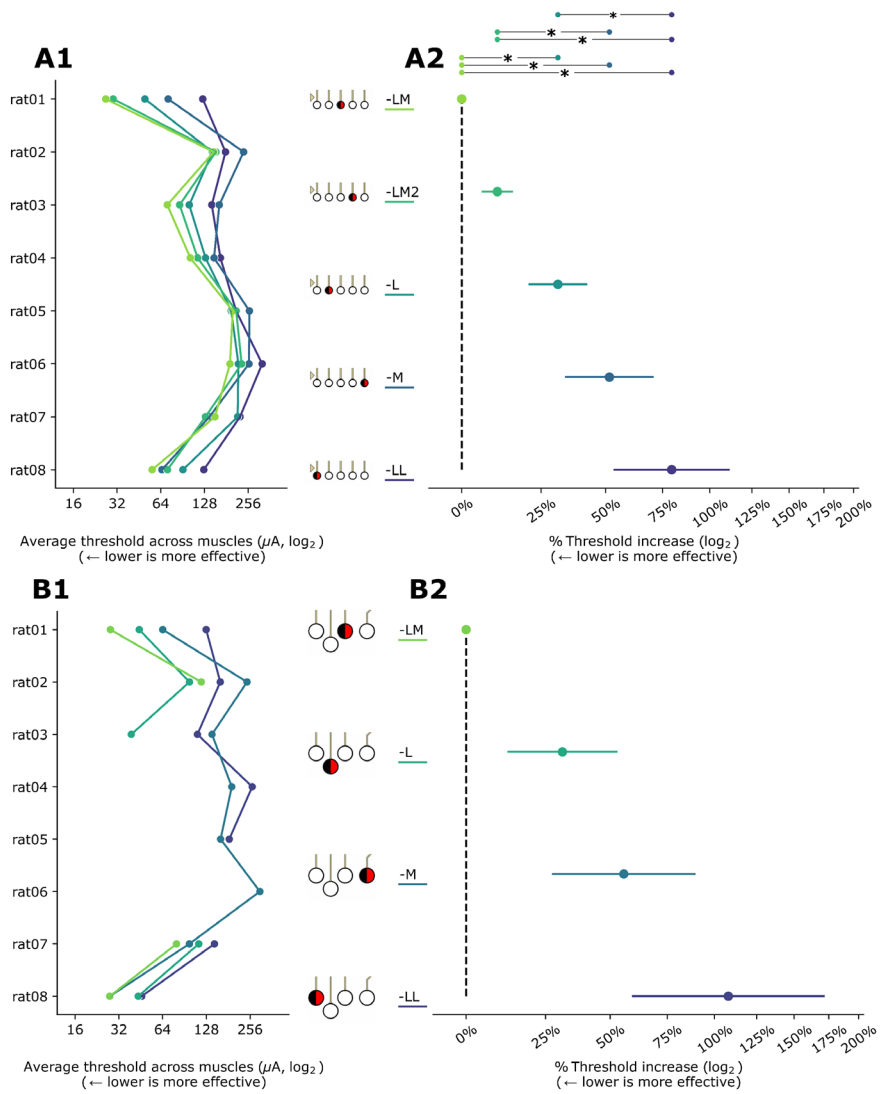

Figure 3. Stimulation over the DREZ is optimal for both small and large contacts on the linear electrode array. (A) For small contacts, the lateromedial position (LM) yields significantly lower thresholds compared to lateral (L), medial (M), and far lateral (LL) positions. The second lateromedial position (LM2), located between LM and M, is the second most effective. Overall, efficacy decreases as the contact position moves away from LM, with the ranking from most to least effective: LM, LM2, L, M, LL. **(B)** Same as (A), but for large contacts, which follow the same efficacy ranking. B1: missing line segments indicate rats that were not tested at certain positions due to high impedance.

Since electrodes were designed on a shared coordinate system, comparable mediolateral positions could be identified and tested across array types (Fig. 4E). Contacts on the circular array were labeled using a cardinal coordinate system, and positions corresponding to the optimal laterality on the linear array (LM for both large and small contacts) included the center (C), north (N), and south (S) contacts, which were also aligned with the DREZ.

The south contact (S) was most effective, followed by center (C) and north (N) (Fig. 4, Supplementary Fig. S3). While these three lateromedial contacts were more effective than the most medial and far lateral contacts, differences among S, C, and N were not statistically significant. The most medial contact (East, E) (Fig. 1D) was least effective, with thresholds 118% higher than S (1.126 ± 0.324, $p = 0.039$), 95% higher than C (0.965 ± 0.265, $p = 0.039$), and 72% higher than N (0.781 ± 0.263, $p = 0.053$). The far lateral contact (West, W) showed similarly low efficacy as E, with thresholds 112% higher than S (1.081 ± 0.275, $p = 0.039$), 89% higher than C (0.921 ± 0.237, $p = 0.039$), and 67% higher than N (0.736 ± 0.214, $p = 0.039$).

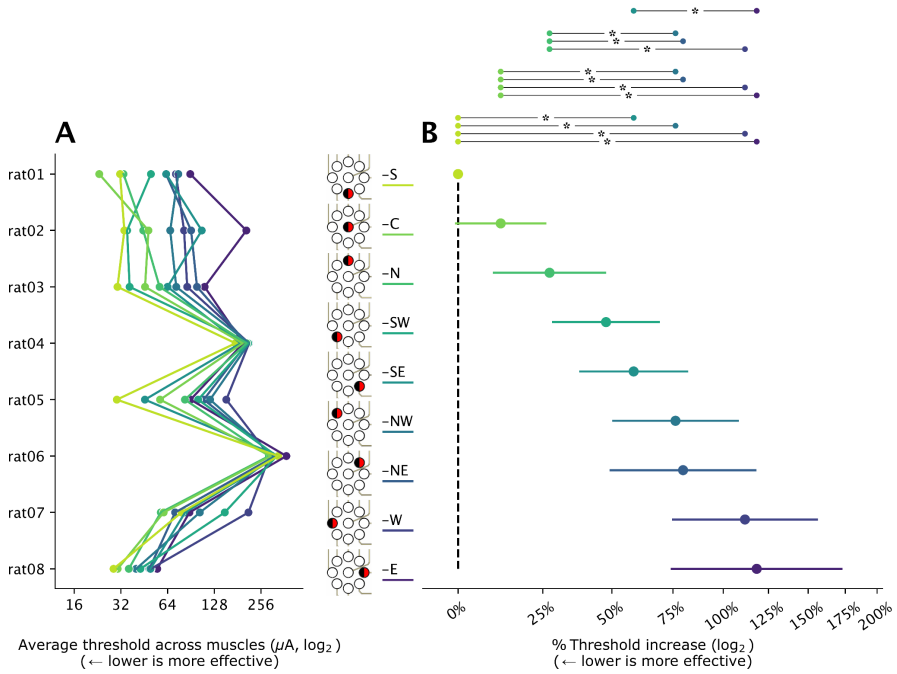

Figure 4. Position of circular electrodes aligned over the DREZ is optimal. (A) Average thresholds across six tested muscles for each of the 8 rats tested. Line colors correspond to electrode positions shown in (B). **(B)** Contacts aligned over the DREZ, south (S), center (C), and north (N), are most effective and result in lower thresholds, with S being the most effective. Contacts are labeled by their cardinal coordinates. Midline (East, E) and far lateral (West, W) contacts are least effective, while intercardinal contacts show intermediate efficacy. Overall, efficacy increases as the position approaches the lateromedial axis aligned over the DREZ.

Intercardinal contacts (NE, NW, SE, SW) showed intermediate efficacy and resulted in lower thresholds than E and W, but these differences did not reach statistical significance in most comparisons. Notably, thresholds for E were 38% higher than SE (0.464 ± 0.141, $p = 0.043$), and thresholds for W were 44% higher than SW (0.524 ± 0.179, $p = 0.053$). Differences within the intercardinal contacts were not significant. Overall, efficacy ranked from highest to lowest as: S, C, N, SW, SE, NW, NE, W, and E. See Supplementary Fig. S3 for all pairwise comparisons and Supplementary Fig. S4 for corresponding Bayesian analysis.

3.2 Orientation: Rostro-Caudal is most effective

The circular electrode configuration was designed to assess how current orientation influences stimulation efficacy by delivering current between two contacts centered over the DREZ. We hypothesized that stimulation oriented perpendicular to the entering root would be most effective. To test this, we compared four major orientations using opposing contact pairs on the circular array: rostro-caudal (S-N contacts), latero-medial (E-W), root-aligned (NE-SW), and root-perpendicular (SE-NW) (Fig. 5).

Rostro-caudal orientation was most effective (Fig. 5, Supplementary Fig. S5). Relative to it, thresholds increased by 141% for latero-medial (1.269 ± 0.165, $p = 0.0007$), 76% for root-aligned (0.816 ± 0.167, $p = 0.004$), and 68% for root-perpendicular (0.752 ± 0.146, $p = 0.004$). Latero-medial was also significantly less effective than both root-perpendicular (43% increase, 0.517 ± 0.16, $p = 0.022$), and root-aligned (37%, 0.453 ± 0.15, $p = 0.023$). No significant difference was observed between root-aligned and root-perpendicular. Overall, efficacy ranked from highest to lowest as: S-N, SE-NW, NE-SW, E-W. See Supplementary Fig. S5 for all pairwise comparisons and Supplementary Fig. S6 for corresponding Bayesian analysis.

To further validate the optimal orientation, we tested radial bipolar configurations with the primary contact fixed at the center and the return positioned at one of the eight surrounding cardinal contacts. This design ensured consistent positioning of one contact across conditions. The south-center (S-C) configuration was most effective, followed by north-center (N-C) (Supplementary Fig. S7, Supplementary Fig. S8). Relative to S-C, thresholds were significantly higher for E-C (68%, 0.752 ± 0.095, $p = 0.012$), W-C (67%, 0.743 ± 0.167, $p = 0.020$), SE–C (55%, 0.632 ± 0.105, $p = 0.012$), NE-C (48%, 0.569 ± 0.172, $p = 0.044$), and NW-C (24%, 0.540 ± 0.132, $p = 0.024$). Thresholds were also higher for SW-C (24%, 0.314 ± 0.120, $p = 0.080$) and N-C (23%, 0.300 ± 0.122, $p = 0.093$). The intercardinal configurations showed intermediate efficacy, with the overall ranking from most to least effective: S-C, N-C, SW-C, NW-C, NE-C, SE-C, W-C, E-C, consistent with the efficacy in Results 3.2. See Supplementary Fig. S8 for all pairwise comparisons, and Supplementary Fig. S9 for corresponding Bayesian analysis.

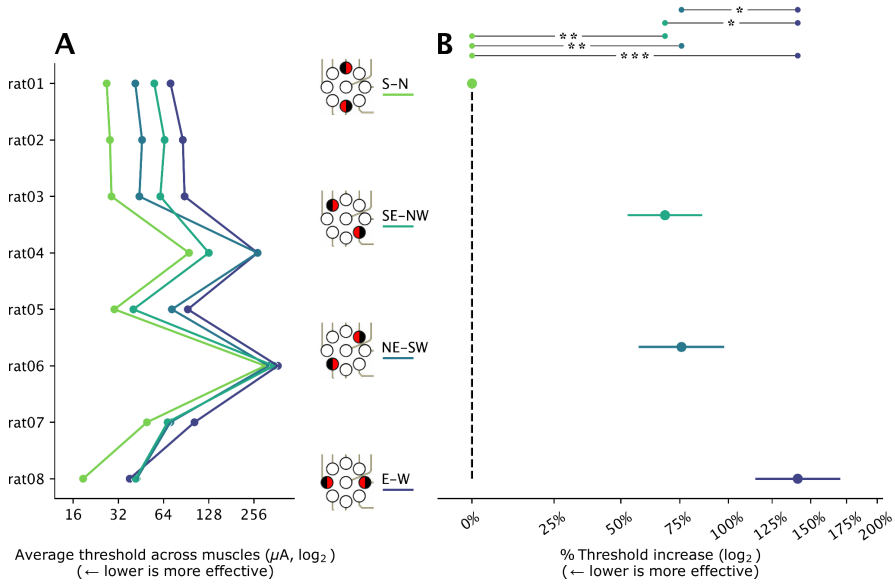

Figure 5. Rostro-caudal orientation is optimal on the circular electrode array. (A) Average thresholds across six tested muscles for each of the 8 rats tested. Line colors correspond to orientations shown in (B). **(B)** The rostro-caudal (S-N) orientation results in significantly lower thresholds compared to latero-medial (E-W), root-aligned (NE-SW), and root-perpendicular (SE-NW). Root-aligned and root-perpendicular orientations have intermediate efficacy, with latero-medial being least effective.

3.3 Size: Larger electrodes are more effective

We hypothesized that contacts with increased surface area would require lower stimulation intensities to evoke an MEP. To test this, we compared large and small contacts at corresponding mediolateral positions, tested at the same segment: M large vs. M small, LM large vs. LM small, L large vs. L small, and LL large vs. LL small (Fig. 6).

Large contacts were significantly more effective than small contacts at the lateral (L) position, where small contacts resulted in 81% higher thresholds (0.857 ± 0.177, $p = 0.034$). At the remaining positions, a similar trend was observed but did not reach statistical significance. Given the reduced sample size resulting from the loss of some large contacts, we further assessed the effect of contact size using a Bayesian framework, which indicated, with high probability, that large contacts were consistently more effective than small contacts across all positions (Supplementary Fig. S10, probability 1.00 at L and LM, 0.99 at M, and 0.95 at LL). There were no significant differences in selectivity between large and small electrodes at any mediolateral position (data not shown).

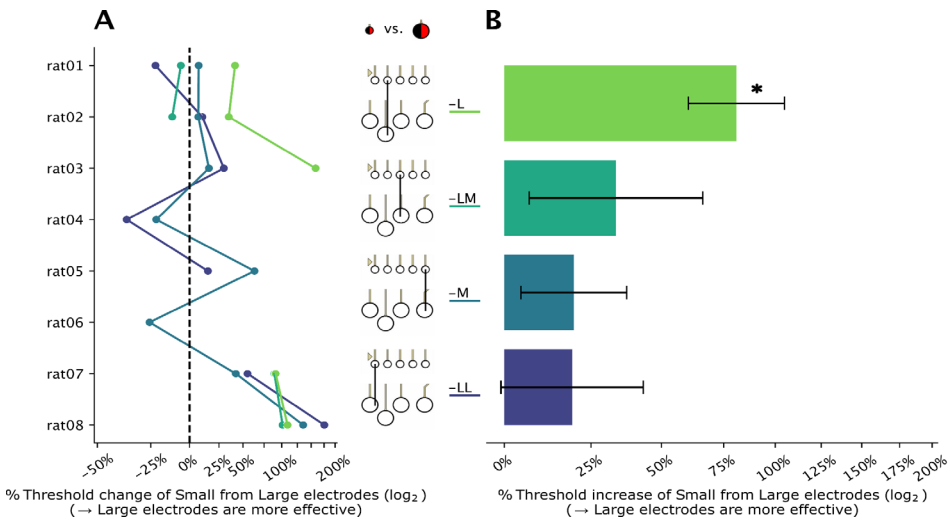

Figure 6. Large electrodes are more effective than small electrodes. (A) Threshold differences between large and small electrode contacts are shown for each of the 8 rats tested. Line colors correspond to differences at similar mediolateral positions shown in (B). Missing line segments indicate positions not tested in certain rats due to high impedance. Positive values indicate that large contacts yielded lower thresholds than small electrodes. **(B)** At the lateral (L) position, large contacts resulted in significantly lower thresholds compared to small contacts.

3.4 High-Definition does not alter selectivity and may decrease efficacy

To assess whether increasing focality around the DREZ may affect generation of MEPs and motor recruitment, we tested high-definition (HD) configurations using the circular electrode array. These configurations used a central electrode surrounded by four return electrodes, similar to HD montages used in brain stimulation (Datta et al. 2009). We hypothesized that concentrating current over the DREZ with an HD arrangement would increase selectivity.

We evaluated multiple configurations with both biphasic and pseudomonophasic pulses (Fig. 7). Using pseudomonophasic pulses, an anode center, both with a distant return or with HD surrounding cathodes, was the least effective (Fig. 7). In contrast, a cathodal center with a distant return was more effective than a cathodal center with HD surrounding anodes (-0.379 ± 0.117, $p = 0.033$). For biphasic stimulation, there were no significant differences between distant return and HD configurations.

Overall, the main consistent effect observed was the polarity dependence with pseudomonophasic stimulation, with cathode center yielding lower thresholds than anode center. HD stimulation did not improve efficacy over a distant return, and in some cases reduced it. No differences in selectivity were observed between any of the tested configurations (data not shown).

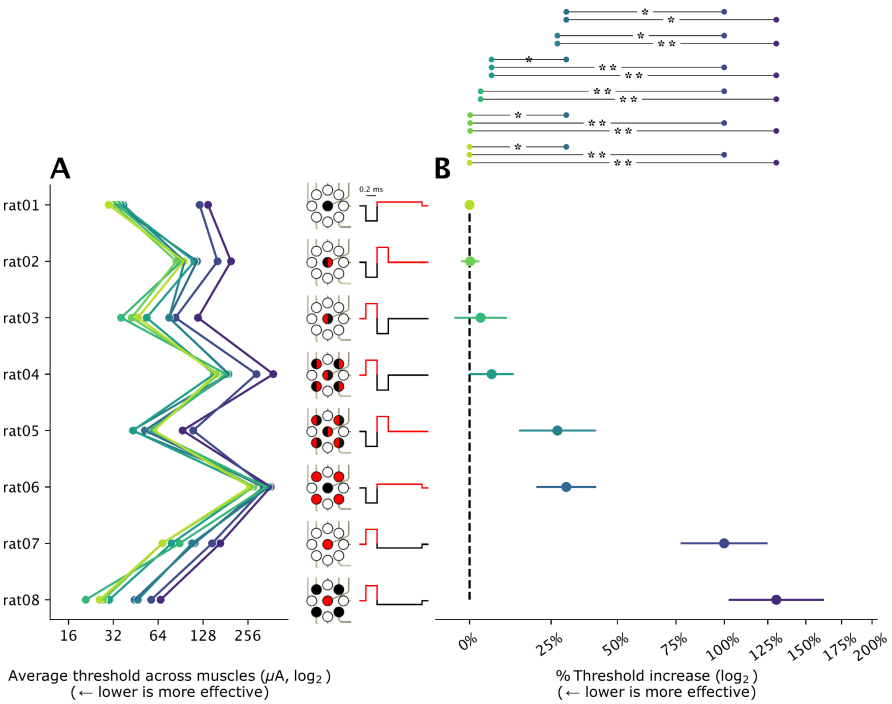

Figure 7. Cathodal stimulation is more effective than anodal stimulation and high-definition montage does not improve efficacy over distant return. (A) Average thresholds across six tested muscles for each of the 8 rats tested. Line colors correspond to waveforms and electrodes shown in (B). **(B)** With pseudomonophasic stimulation, a cathode center is more effective than an anode center, both with distant return and high-definition montage. In contrast, biphasic stimulation shows minimal dependence on polarity, and high-definition montage does not improve efficacy compared to distant return.

3.5 Position and orientation are critical parameters

Experiments were performed in groups to evaluate optimal electrode position, orientation, and waveform. However, we also compared across all tested configurations to assess which parameters had the greatest influence on efficacy. Position and orientation emerged as the most important factors, with the rostro-caudal S-N configuration being the most effective (Supplementary Fig. S13). While the S-N and S-C configurations were not significantly different ($p = 0.074$), the S-N configuration was significantly more effective ($p < 0.05$) than all other tested configurations, including all monopolar and high-definition montages. As expected, the least effective configurations were those where anodal stimulation was applied over the DREZ.

4 Discussion

Epidural spinal cord stimulation experiments using customized arrays advanced our understanding of targeting forelimb motor responses in rats with 4 major conclusions. First, for position in the medio-lateral plane, the DREZ is the most effective location to elicit MEPs with extension in both the medial or lateral direction leading to significant loss of efficacy. Second, for orientation, MEP threshold is minimized when the stimulation vector is parallel to the long axis of the spinal cord. Third, for size, electrode contacts with larger surface areas increase the efficacy of stimulation. Fourth, for waveform cathodal stimulation was superior to anodal stimulation, while a high-definition stimulation paradigm decreased efficacy compared to pairs of stimulating electrodes.

Stimulation over the DREZ had the lowest MEP thresholds compared to stimulation both more medial and further lateral. This agrees with our previous work and that of others that has shown that targeting the DREZ in the cervical spinal cord with dorsal epidural stimulation generates the largest MEPs (Mishra et al. 2017; Greiner et al. 2021; McIntosh et al. 2023). In a finite element model of epidural stimulation of the lumbar spine, Rattay et al. 2000 demonstrated anatomical hotspots both at the region of sharp curvature just before entry to the spinal cord and the actual point of entry (DREZ) (Rattay et al. 2000). Therefore, the local change in fiber orientation at the DREZ may provide the ideal environment for electrical stimulation with locations more lateral or medial lacking this change and requiring elevated intensities.

Electrical current vector-dependent motor responses have been extensively demonstrated in cortical stimulation studies (Foerster et al. 2019; Rawji et al. 2018; Reijonen et al. 2020; Janssen et al. 2015). In the spinal cord, computational models have demonstrated the importance of direction of the electrical field relative to the underlying axonal fibers (Coburn and Sin 1985; Struijk et al. 1993; Coburn 1985). We predicted that electrical current aligned to the root entry would be most effective, however, we found that stimulation of the spinal cord parallel to its long axis yielded the lowest threshold (most effective) MEPs. This potentially speaks to a relatively larger influence on efficacy by the proximity of contacts to the DREZ rather than to the alignment of the dorsal fibers that target it. This is likely influenced by the electrical field orientation relative to the underlying neural elements (Rattay 1986; Ladenbauer et al. 2010; Capogrosso et al. 2013) and the properties of the anatomical structure (Geddes and Baker 1967; Ladenbauer et al. 2010). Previous groups have lacked the contact density in arrays to comprehensively assess the impact of electrode orientation. Our circular array contained contacts designed to align parallel and perpendicular to both the spinal cord and the dorsal roots. We found that an electrical current vector parallel to the spinal cord yields the most effective stimulation.

For electrode size, larger electrodes (500 microns in diameter) decreased the stimulation threshold compared with smaller electrodes (250 microns). Electrode size may not significantly affect the magnitude

of the electrical field generated, but larger electrodes improve field uniformity (Troughton et al. 2023), and this in turn may influence the activated neural structures. Further studies will be needed to determine whether there is a trade off between efficacy (favors large electrodes) and selectivity of the muscles innervated at the stimulated level (may be more specific with smaller electrodes). As our understanding of the interaction between electrical currents and spinal cord anatomy grows, there may be opportunities to design epidural electrodes and waveforms to better engage spinal circuits.

There are a few limitations of this study worth noting. Some comparisons, especially of the large linear electrodes, were limited by the number of rats with successful recruitment curves. This may be due to the array shifting during the experiment or being slightly off center during initial placement leaving some contacts only partially in contact with the spinal cord. However, a clear relationship was observed with large contacts showing increased efficacy of stimulation. In addition, our customized arrays relied on anatomical landmarks for appropriate positioning of the electrode with visual but no radiographic confirmation. We are currently generating new arrays for subsequent experiments that contain radiopaque fiducials to confirm proper placement with x-ray. This will be particularly important for experiments conducted in awake rats. Although the current studies were performed in anesthetized rats, previous studies showed very similar effects of spinal cord stimulation in rats anesthetized with ketamine and xylazine compared with awake rats (Mishra et al. 2017; Pal et al. 2022).

The parameter space available for exploration and optimization in epidural spinal cord stimulation (SCS) is immense. Our electrodes were designed to test parameters within a spinal segment. Future studies should examine the interaction of stimulation across segments, similar to what we have done in mapping the human spinal cord (McIntosh et al. 2023). Given a single combination of parameters is unlikely to be universally optimal, future studies should investigate how these parameters interact to better understand their combinatorial effects. Additionally, some parameters are fundamentally linked. For example, it is not possible to change orientation of current flow without simultaneously changing the position of the active electrodes. Advances in implantable technologies could improve both the delivery of electrical current and measurement of the effects through sensing electrodes. Measurement of spinal cord extracellular compound action potentials could serve as real-time physiological biomarkers to guide stimulation parameter selection. This approach may ultimately enable tailored stimulation strategies to support functional recovery, such as finding optimal stimulation paradigms for recovery of reaching or grasping movements in patients with loss of arm and hand function.

This study demonstrates the potential for customized electrodes to improve our understanding of dorsal epidural stimulation through targeted experiments with arrays designed to assess specific questions. If these configurations prove more effective than conventional geometries, then they could improve clinical devices. Higher efficacy would yield similar effects of stimulation at lower intensity. Lower currents mean

less draw on the batteries of implantable devices, which could mean longer times between charges for patients with these devices. Future studies may assess the trade-off between efficacy and selectivity for various epidural stimulation paradigms and the optimization of epidurally implanted electrode arrays in humans.

5 Additional information

5.1 Competing interests

Jason B. Carmel is a Founder and stockholder in BackStop Neural and a scientific advisor and stockholder in SharperSense. Walter Voit co-founded several neuromodulation companies including Qualia Oto, Backstop Neural, and Kardiodia which have licenses to technology developed at UT Dallas. The other authors have nothing to disclose.

5.1.1 Funding

This work was supported by the National Institute of Neurological Disorders and Stroke, National Institutes of Health (award R01NS124224, 1R03NS141040), and a Department of Health New York State Institutional Grant (award C38336GG), and by the Congressionally Directed Medical Research Program (award HT9425-24-1-0218).

5.1.2 Acknowledgements

We thank Jacob Kang for assistance during experiments and Windsor Ting and Maria Bandres for comments.

5.1.3 Author contributions

Conceptualization: ASA, JRM, JBC; Data Curation: VT, JRM; Formal Analysis: AP, VT, ASA, JRM; Funding Acquisition: WEV, JRM, JBC; Investigation: ASA; Methodology: ASA, PER, OR, WEV, JRM, JBC; Resources: PER, OR, WEV, JBC; Software: AP, VT, JRM; Supervision: WEV, JRM, JBC; Validation: AP, VT, ASA, JRM; Visualization: AP, VT, PER; Writing - Original Draft: AP, VT; Writing - Review & Editing: AP, VT, ASA, PER, OR, WEV, JRM, JBC.

5.1.4 Data and code availability

The datasets used in this study are available from the corresponding authors upon reasonable request. The code to reproduce the presented analyses is available at https://github.com/hbmep/rat-mapping.

6 References

Alam, Monzurul, Guillermo Garcia-Alias, Benita Jin, et al. 2017. "Electrical Neuromodulation of the Cervical Spinal Cord Facilitates Forelimb Skilled Function Recovery in Spinal Cord Injured Rats." *Experimental Neurology* 291 (May): 141–50. https://doi.org/10.1016/j.expneurol.2017.02.006.

Alam, Monzurul, Guillermo Garcia-Alias, Prithvi K. Shah, et al. 2015. "Evaluation of Optimal Electrode Configurations for Epidural Spinal Cord Stimulation in Cervical Spinal Cord Injured Rats." *Journal of Neuroscience Methods* 247 (May): 50–57. https://doi.org/10.1016/j.jneumeth.2015.03.012.

Benjamini, Yoav, and Yosef Hochberg. 1995. "Controlling the False Discovery Rate: A Practical and Powerful Approach to Multiple Testing." *Journal of the Royal Statistical Society: Series B (Methodological)* 57 (1): 289–300. https://doi.org/10.1111/j.2517-6161.1995.tb02031.x.

Capogrosso, Marco, Nikolaus Wenger, Stanisa Raspopovic, et al. 2013. "A Computational Model for Epidural Electrical Stimulation of Spinal Sensorimotor Circuits." *The Journal of Neuroscience* 33 (49): 19326–40. https://doi.org/10.1523/JNEUROSCI.1688-13.2013.

Coburn, Barry. 1985. "A Theoretical Study of Epidural Electrical Stimulation of the Spinal Cord - Part II: Effects on Long Myelinated Fibers." *IEEE Transactions on Biomedical Engineering* BME-32 (11): 978–86. https://doi.org/10.1109/TBME.1985.325649.

Coburn, Barry, and Wing Kee Sin. 1985. "A Theoretical Study of Epidural Electrical Stimulation of the Spinal Cord Part I: Finite Element Analysis of Stimulus Fields." *IEEE Transactions on Biomedical Engineering* BME-32 (11): 971–77. https://doi.org/10.1109/TBME.1985.325648.

Cuellar, Carlos, Lauri Lehto, Riaz Islam, Silvia Mangia, Shalom Michaeli, and Igor Lavrov. 2024. "Selective Activation of the Spinal Cord with Epidural Electrical Stimulation." *Brain Sciences* 14 (7): 650. https://doi.org/10.3390/brainsci14070650.

Datta, Abhishek, Varun Bansal, Julian Diaz, Jinal Patel, Davide Reato, and Marom Bikson. 2009. "Gyri-Precise Head Model of Transcranial Direct Current Stimulation: Improved Spatial Focality Using a Ring Electrode versus Conventional Rectangular Pad." *Brain Stimulation* 2 (4): 201–7, 207.e1. https://doi.org/10.1016/j.brs.2009.03.005.

Datta, Abhishek, Maged Elwassif, Fortunato Battaglia, and Marom Bikson. 2008. "Transcranial Current Stimulation Focality Using Disc and Ring Electrode Configurations: FEM Analysis." *Journal of Neural Engineering* 5 (2): 163–74. https://doi.org/10.1088/1741-2560/5/2/007.

Foerster, Águida, Fatemeh Yavari, Leila Farnad, et al. 2019. "Effects of Electrode Angle-Orientation on the Impact of Transcranial Direct Current Stimulation on Motor Cortex Excitability." *Brain Stimulation* 12 (2): 263–66. https://doi.org/10.1016/j.brs.2018.10.014.

Garcia-Sandoval, Aldo, Ajay Pal, Asht M Mishra, et al. 2018. "Chronic Softening Spinal Cord Stimulation Arrays." *Journal of Neural Engineering* 15 (4): 045002. https://doi.org/10.1088/1741-2552/aab90d.

Geddes, L. A., and L. E. Baker. 1967. "The Specific Resistance of Biological Material—A Compendium of Data for the Biomedical Engineer and Physiologist." *Medical and Biological Engineering* 5 (3): 271–93. https://doi.org/10.1007/BF02474537.

Greiner, Nathan, Beatrice Barra, Giuseppe Schiavone, et al. 2021. "Recruitment of Upper-Limb Motoneurons with Epidural Electrical Stimulation of the Cervical Spinal Cord." *Nature Communications* 12 (1): 1. https://doi.org/10.1038/s41467-020-20703-1.

Holsheimer, J., J. J. Struijk, and N. R. Tas. 1995. "Effects of Electrode Geometry and Combination on Nerve Fibre Selectivity in Spinal Cord Stimulation." *Medical and Biological Engineering and Computing* 33 (5): 676–82. https://doi.org/10.1007/BF02510785.

Janssen, Arno M., Thom F. Oostendorp, and Dick F. Stegeman. 2015. "The Coil Orientation Dependency of the Electric Field Induced by TMS for M1 and Other Brain Areas." *Journal of NeuroEngineering and Rehabilitation* 12 (1): 47. https://doi.org/10.1186/s12984-015-0036-2.

Ladenbauer, Josef, Karen Minassian, Ursula S. Hofstoetter, Milan R. Dimitrijevic, and Frank Rattay. 2010. "Stimulation of the Human Lumbar Spinal Cord with Implanted and Surface Electrodes: A Computer Simulation Study." *IEEE Transactions on Neural Systems and Rehabilitation Engineering: A Publication of the IEEE Engineering in Medicine and Biology Society* 18 (6): 637–45. https://doi.org/10.1109/TNSRE.2010.2054112.

Lloyd, David P. C. 1943. "Reflex Action in Relation to Pattern and Peripheral Source of Afferent Stimulation." *Journal of Neurophysiology* 6 (2): 111–19. https://doi.org/10.1152/jn.1943.6.2.111.

Mao, Guang-Wei, Jian-Jun Zhang, Hao Su, et al. 2022. "A Flexible Electrode Array for Determining Regions of Motor Function Activated by Epidural Spinal Cord Stimulation in Rats with Spinal Cord Injury." *Neural Regeneration Research* 17 (3): 601. https://doi.org/10.4103/1673-5374.320987.

McIntosh, James R., Evan F. Joiner, Jacob L. Goldberg, et al. 2023. "Intraoperative Electrical Stimulation of the Human Dorsal Spinal Cord Reveals a Map of Arm and Hand Muscle Responses." *Journal of Neurophysiology* 129 (1): 66–82. https://doi.org/10.1152/jn.00235.2022.

Meacham, Kathleen W., Richard J. Giuly, Liang Guo, Shawn Hochman, and Stephen P. DeWeerth. 2008. "A Lithographically-Patterned, Elastic Multi-Electrode Array for Surface Stimulation of the Spinal Cord." *Biomedical Microdevices* 10 (2): 259–69. https://doi.org/10.1007/s10544-007-9132-9.

Minev, Ivan R., Pavel Musienko, Arthur Hirsch, et al. 2015. "Biomaterials. Electronic Dura Mater for Long-Term Multimodal Neural Interfaces." *Science (New York, N.Y.)* 347 (6218): 159–63. https://doi.org/10.1126/science.1260318.

Mishra, Asht M., Ajay Pal, Disha Gupta, and Jason B. Carmel. 2017. "Paired Motor Cortex and Cervical Epidural Electrical Stimulation Timed to Converge in the Spinal Cord Promotes Lasting Increases in Motor Responses." *The Journal of Physiology* 595 (22): 6953–68. https://doi.org/10.1113/JP274663.

Nandra, Mandheerej. S., Igor A. Lavrov, V. Reggie Edgerton, and Yu-Chong Tai. 2011. "A Parylene-Based Microelectrode Array Implant for Spinal Cord Stimulation in Rats." *2011 IEEE 24th International Conference on Micro Electro Mechanical Systems*, January, 1007–10. https://doi.org/10.1109/MEMSYS.2011.5734598.

North, Richard B., David H. Kidd, John C. Olin, et al. 2002. "Spinal Cord Stimulation Electrode Design: Prospective, Randomized, Controlled Trial Comparing Percutaneous and Laminectomy Electrodes - Part I: Technical Outcomes." *Neurosurgery* 51 (2): 381–90. https://doi.org/10.1097/00006123-200208000-00015.

North, Richard B., David H. Kidd, Loredana Petrucci, and Michael J. Dorsi. 2005. "Spinal Cord Stimulation Electrode Design: A Prospective, Randomized, Controlled Trial Comparing Percutaneous with Laminectomy Electrodes: Part II-Clinical Outcomes." *Neurosurgery* 57 (5): 990–96; discussion 990-996. https://doi.org/10.1227/01.neu.0000180030.00167.b9.

Pal, Ajay, HongGeun Park, Aditya Ramamurthy, et al. 2022. "Spinal Cord Associative Plasticity Improves Forelimb Sensorimotor Function after Cervical Injury." *Brain*, September 2, awac235. https://doi.org/10.1093/brain/awac235.

Rattay, F., K. Minassian, and M. R. Dimitrijevic. 2000. "Epidural Electrical Stimulation of Posterior Structures of the Human Lumbosacral Cord: 2. Quantitative Analysis by Computer Modeling." *Spinal Cord* 38 (8): 473–89. https://doi.org/10.1038/sj.sc.3101039.

Rattay, Frank. 1986. "Analysis of Models for External Stimulation of Axons." *IEEE Transactions on Biomedical Engineering* BME-33 (10): 974–77. https://doi.org/10.1109/TBME.1986.325670.

Rattay, Frank, Simon M. Danner, Ursula S. Hofstoetter, and Karen Minassian. 2014. "Finite Element Modeling for Extracellular Stimulation." In *Encyclopedia of Computational Neuroscience*, edited by Dieter Jaeger and Ranu Jung. Springer New York. https://doi.org/10.1007/978-1-4614-7320-6_593-5.

Rawji, Vishal, Matteo Ciocca, André Zacharia, et al. 2018. "tDCS Changes in Motor Excitability Are Specific to Orientation of Current Flow." *Brain Stimulation* 11 (2): 289–98. https://doi.org/10.1016/j.brs.2017.11.001.

Reijonen, Jusa, Laura Säisänen, Mervi Könönen, Ali Mohammadi, and Petro Julkunen. 2020. "The Effect of Coil Placement and Orientation on the Assessment of Focal Excitability in Motor Mapping with Navigated Transcranial Magnetic Stimulation." *Journal of Neuroscience Methods* 331 (February): 108521. https://doi.org/10.1016/j.jneumeth.2019.108521.

Renshaw, Birdsey. 1940. "Activity in the Simplest Spinal Reflex Pathways." *Journal of Neurophysiology* 3 (5): 373–87. https://doi.org/10.1152/jn.1940.3.5.373.

Rocha-Flores, Pedro E., Chandani Chitrakar, Ovidio Rodriguez-Lopez, et al. 2025. "Softening, Conformable, and Stretchable Conductors for Implantable Bioelectronics Interfaces." *Advanced Materials Technologies* 10 (6): 2401047. https://doi.org/10.1002/admt.202401047.

Rocha-Flores, Pedro Emanuel, Edgar Guerrero, Ovidio Rodríguez-Lopez, et al. 2023. "Softening and Flexible Hybrid Electronics Integration for Biomedical Applications." *MRS Communications* 13 (5): 892–900. https://doi.org/10.1557/s43579-023-00431-5.

Russman, Samantha M., Rhea Montgomery-Walsh, Ritwik Vatsyayan, et al. 2025. "The Conformal, High-Density SpineWrap Microelectrode Array for Focal Stimulation and Selective Muscle Recruitment." *Advanced Functional Materials* 35 (16): 2420488. https://doi.org/10.1002/adfm.202420488.

Sharma, Pawan, and Prithvi K. Shah. 2021. "In Vivo Electrophysiological Mechanisms Underlying Cervical Epidural Stimulation in Adult Rats." *The Journal of Physiology* 599 (12): 3121–50. https://doi.org/10.1113/JP281146.

Struijk, J. J., J. Holsheimer, and H. B. Boom. 1993. "Excitation of Dorsal Root Fibers in Spinal Cord Stimulation: A Theoretical Study." *IEEE Transactions on Bio-Medical Engineering* 40 (7): 632–39. https://doi.org/10.1109/10.237693.

Troughton, Joe G., Yaw O. Ansong, Nida Duobaite, and Christopher M. Proctor. 2023. *Finite Element Analysis of Electric Field Distribution during Direct Current Stimulation of the Spinal Cord: Implications for Device Design.* December. https://doi.org/10.1063/5.0163264.

Tyagi, Vishweshwar, Lynda M. Murray, Ahmet S. Asan, et al. 2024. "Hierarchical Bayesian Estimation of Motor-Evoked Potential Recruitment Curves Yields Accurate and Robust Estimates." arXiv:2407.08709. Preprint, arXiv, July 11. https://doi.org/10.48550/arXiv.2407.08709.

Virtanen, Pauli, Ralf Gommers, Travis E. Oliphant, et al. 2020. "SciPy 1.0: Fundamental Algorithms for Scientific Computing in Python." *Nature Methods* 17 (3): 261–72. https://doi.org/10.1038/s41592-019-0686-2.

Wecht, Jaclyn R., William M. Savage, Grace O. Famodimu, et al. 2021. "Posteroanterior Cervical Transcutaneous Spinal Cord Stimulation: Interactions with Cortical and Peripheral Nerve Stimulation." *Journal of Clinical Medicine* 10 (22): 5304. https://doi.org/10.3390/jcm10225304.

Wenger, Nikolaus, Eduardo Martin Moraud, Jerome Gandar, et al. 2016. "Spatiotemporal Neuromodulation Therapies Engaging Muscle Synergies Improve Motor Control after Spinal Cord Injury." *Nature Medicine* 22 (2): 138–45. https://doi.org/10.1038/nm.4025.

Yang, Qi, Aditya Ramamurthy, Sophia Lall, et al. 2019. "Independent Replication of Motor Cortex and Cervical Spinal Cord Electrical Stimulation to Promote Forelimb Motor Function after Spinal Cord Injury in Rats." *Experimental Neurology* 320 (October): 112962. https://doi.org/10.1016/j.expneurol.2019.112962.

Zander, Hans J, Robert D Graham, Carlos J Anaya, and Scott F Lempka. 2020. "Anatomical and Technical Factors Affecting the Neural Response to Epidural Spinal Cord Stimulation." *Journal of Neural Engineering* 17 (3): 036019. https://doi.org/10.1088/1741-2552/ab8fc4.

Zander, Hans J., Krzysztof E. Kowalski, Anthony F. DiMarco, and Scott F. Lempka. 2022. "Model-Based Optimization of Spinal Cord Stimulation for Inspiratory Muscle Activation." *Neuromodulation : Journal of the International Neuromodulation Society* 25 (8): 1317–29. https://doi.org/10.1111/ner.13415.

7 Supplementary information

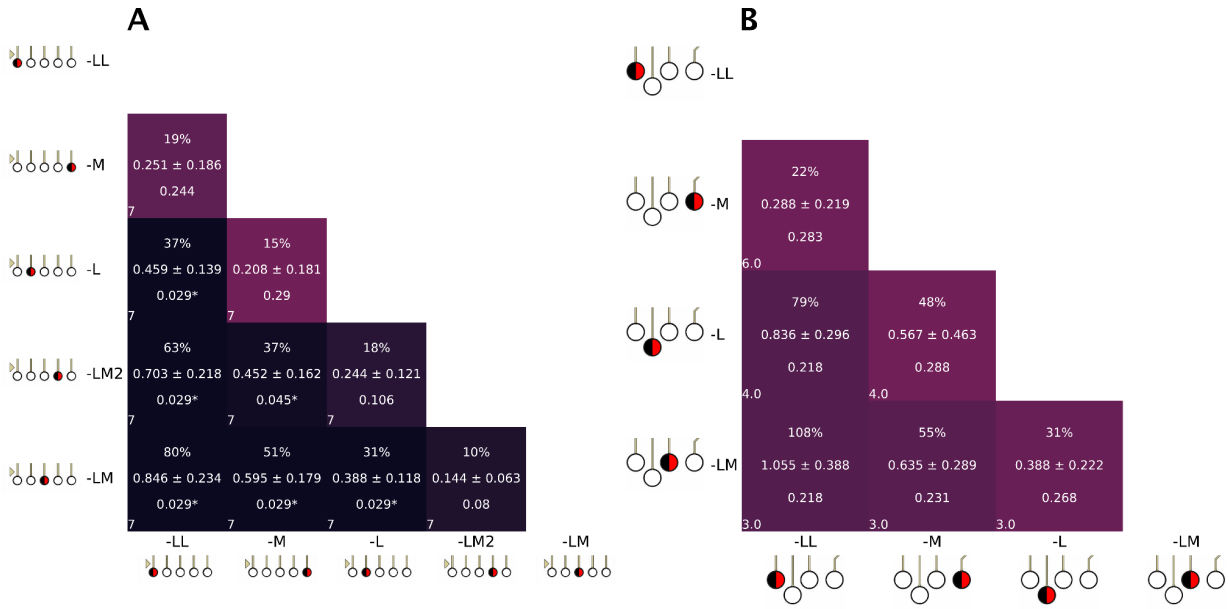

Figure S1. Pairwise efficacy comparison of mediolateral positions for small and large electrodes. (A) Heatmap showing all pairwise comparisons between mediolateral positions for small electrodes in the linear array. Each cell reports the threshold increase of the position in the column relative to the row, with darker cell color indicating lower p-value, after correcting for false discovery rate across all pairwise comparisons. Cells display: (top) percentage increase in threshold of the column relative to the row, (middle) mean threshold difference ± SEM on the $\log_2$ scale, (bottom) corrected p-value, and (bottom left) degrees of freedom for the paired t-test. Rows are ordered based on the number of other positions each beat in head-to-head comparisons, with more effective positions at the bottom. The lateromedial (LM) position was most effective, with significantly lower thresholds compared to the far lateral (LL), medial (M), and lateral (L) positions, and slightly lower (not significant) thresholds compared to the second lateromedial position (LM2). **(B)** Same as (A), but for large electrode contacts. A similar trend is observed, with lateromedial position being more effective. The degrees of freedom are lower due to a reduced number of rats tested, resulting from high-impedance.

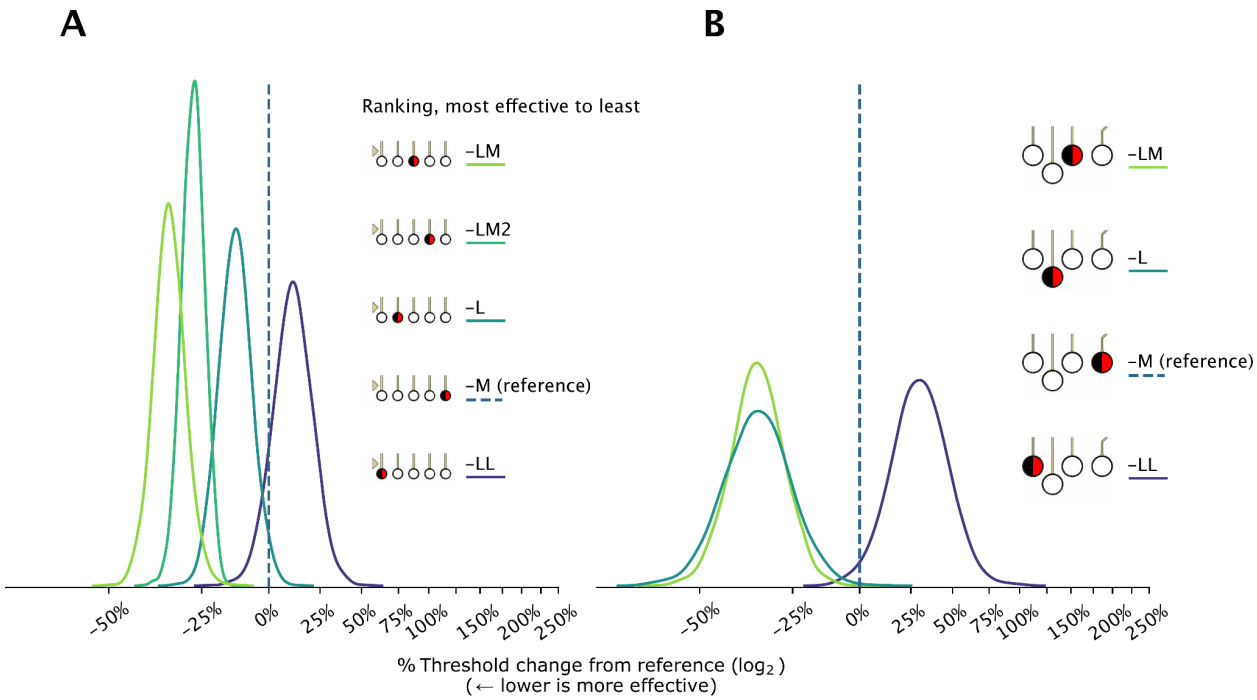

Figure S2. Bayesian comparison of mediolateral positions for large and small electrodes. (A) Each posterior distribution summarizes the threshold change relative to the medial (M) position for small electrodes. Distributions to the left indicate more effective positions (i.e., lower thresholds), with lighter shades of green denoting greater efficacy. LM yields lower thresholds than LM2 with posterior probability 0.89, and lower thresholds than all other positions with probability 1.00. **(B)** LM is comparable to L, and yields lower thresholds than M and LL with probability 1.00.

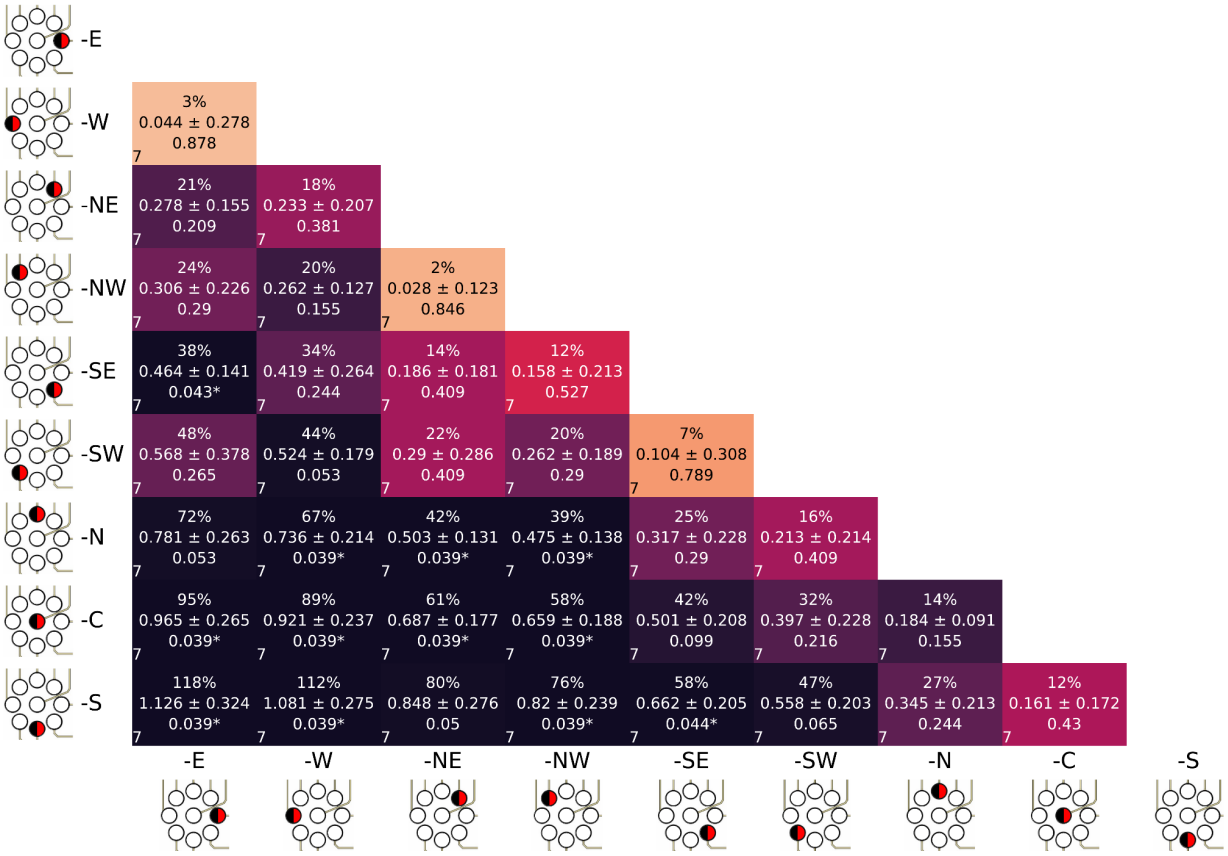

Figure S3. Pairwise efficacy comparison of positions on the circular array. Contacts aligned over the DREZ, south (S), center (C), and north (N), are most effective and result in lower thresholds, with S being the most effective. Overall, efficacy increases as the position approaches the lateromedial axis aligned over the DREZ. Each cell reports the threshold increase of the position in the column relative to the row, with darker cell color indicating lower p-value, after correcting for false discovery rate across all pairwise comparisons. Cells display: (top) percentage increase in threshold of the column relative to the row, (middle) mean threshold difference ± SEM on the $\log_2$ scale, (bottom) corrected p-value, and (bottom left) degrees of freedom for the paired t-test. Rows are ordered based on the number of other positions each beat in head-to-head comparisons, with more effective positions at the bottom.

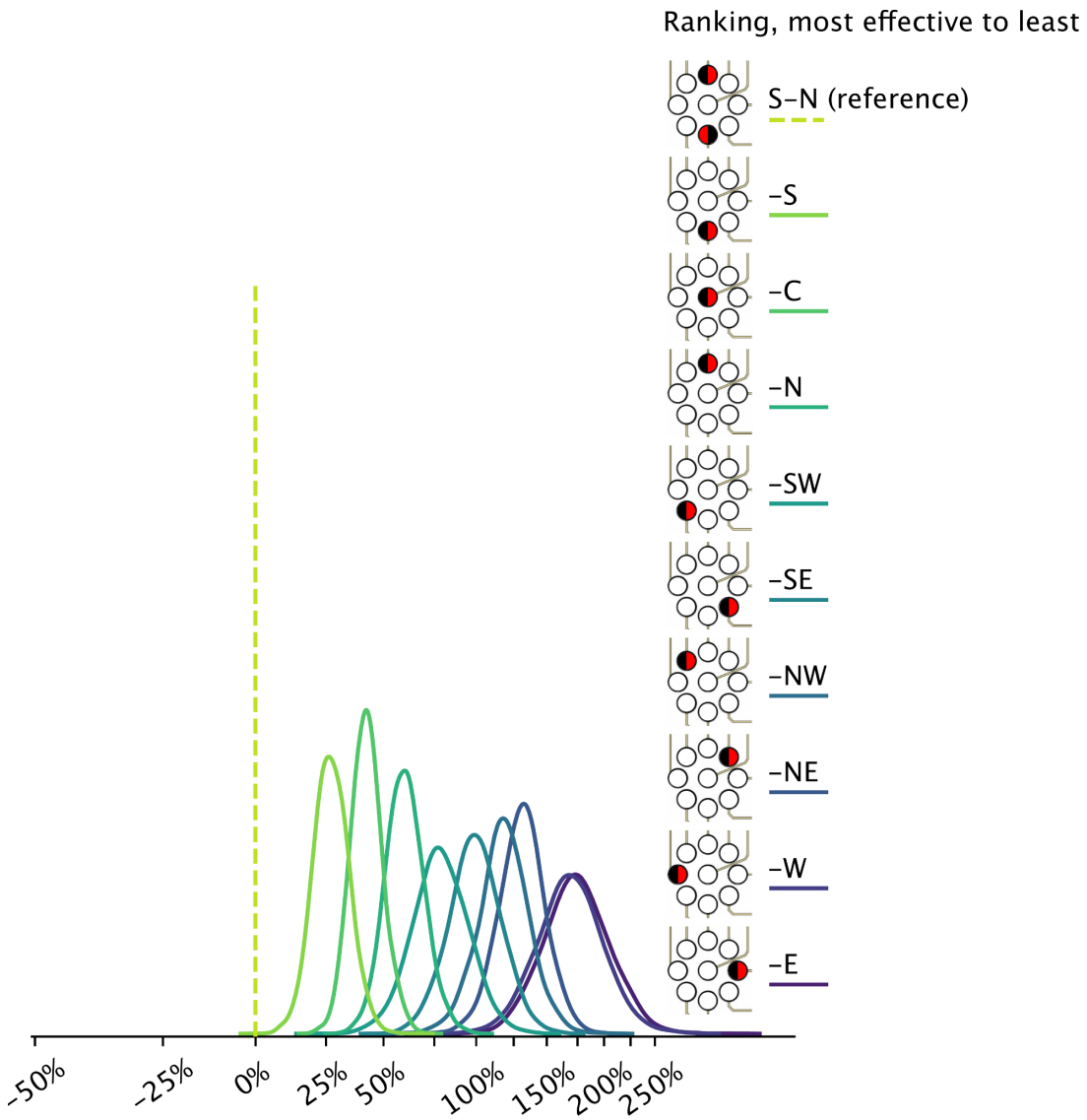

Figure S4. Bayesian comparison of positions on the circular array. Posterior distributions summarize change in threshold relative to the most effective rostro-caudal orientation (S-N). South (S) contact yields lower thresholds than center (C) with probability 0.95, and with probability 1.00 compared to all other positions.

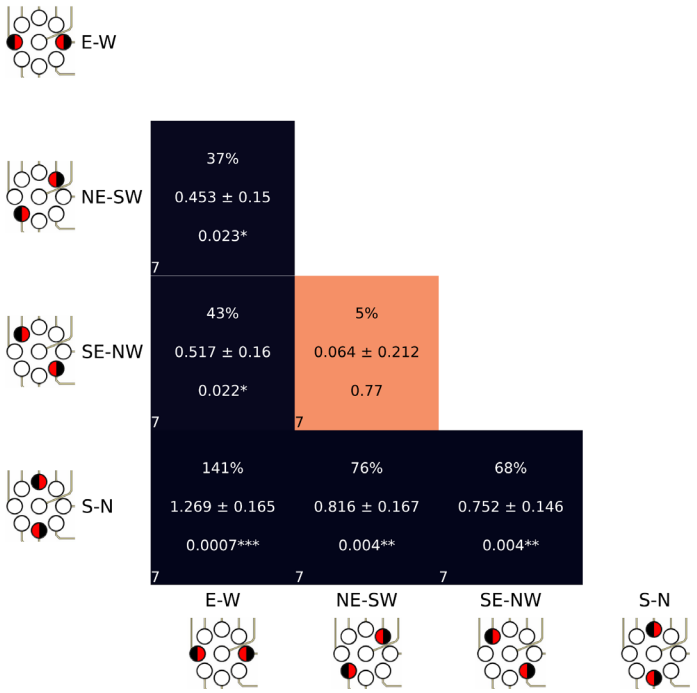

Figure S5. Pairwise efficacy comparison of orientations on the circular array. The rostro-caudal (S-N) orientation results in significantly lower thresholds compared to latero-medial (E-W), root-aligned (NE-SW), and root-perpendicular (SE-NW). Each cell reports the threshold increase of the orientation in the column relative to the row, with darker cell color indicating lower p-value, after correcting for false discovery rate across all pairwise comparisons. Cells display: (top) percentage increase in threshold of the column relative to the row, (middle) mean threshold difference ± SEM on the $\log_2$ scale, (bottom) corrected p-value, and (bottom left) degrees of freedom for the paired t-test. Rows are ordered based on the number of other orientations each beat in head-to-head comparisons, with more effective orientations at the bottom.

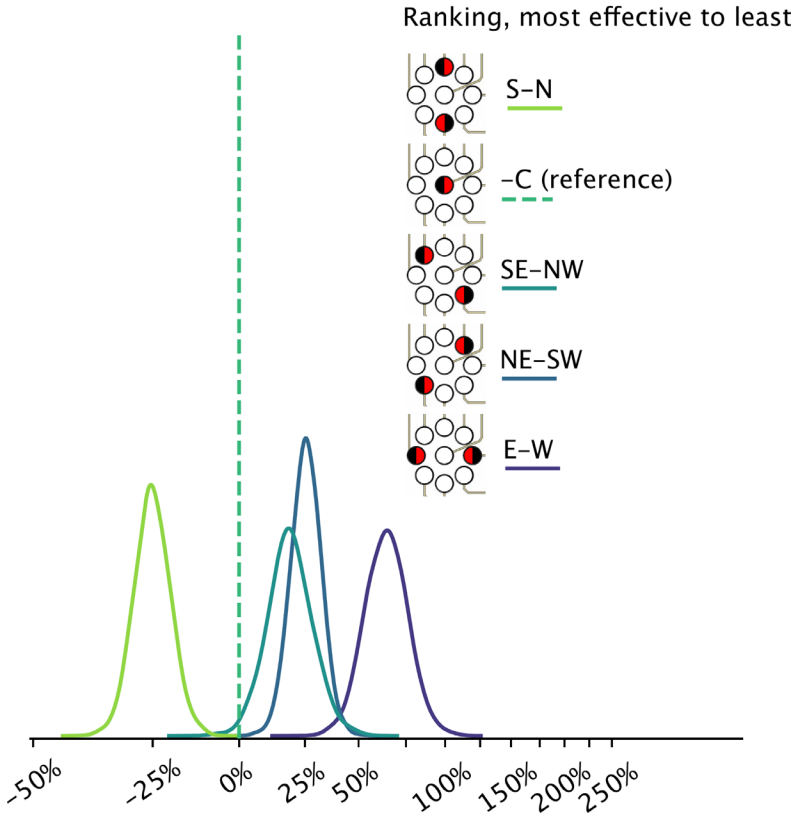

Figure S6. Bayesian comparison of orientations on the circular array. Posterior distributions summarize change in threshold relative to the center (C) contact. The rostro-caudal (S-N) orientation is most effective and yields lower thresholds than all others with posterior probability 1.00.

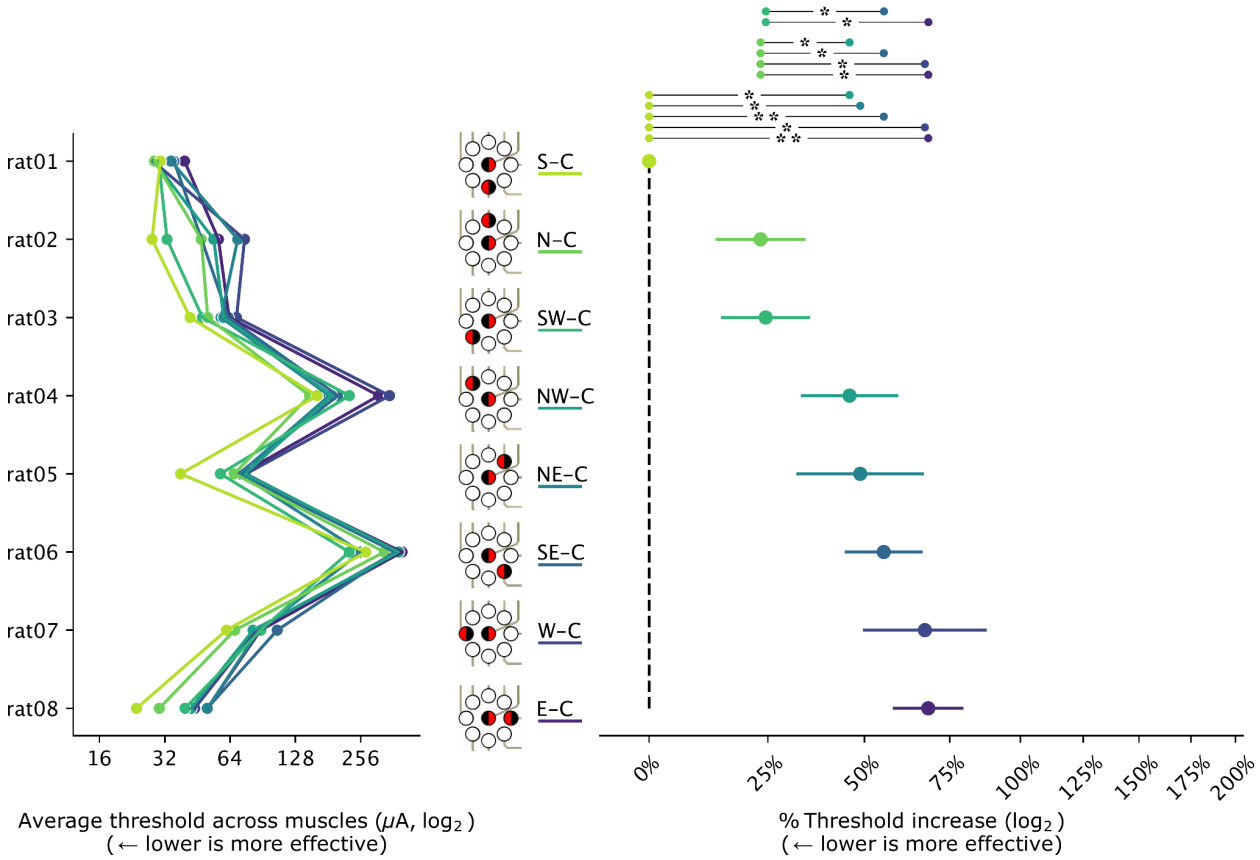

Figure S7. Radial bipolar configurations on the circular array with rostrocaudal alignment over the DREZ are most effective. Pairwise comparisons of radial bipolar configurations with the cathode fixed at the center contact and the anode placed at one of the eight surrounding cardinal or intercardinal contacts. The south-center (S-C) configuration is most effective, followed by north-center (N-C). Mediolateral orientations are least effective, and intercardinal configurations exhibit intermediate efficacy. The resulting order of efficacy is consistent with the broader finding that orientations aligned along the rostrocaudal axis over the DREZ result in lower thresholds.

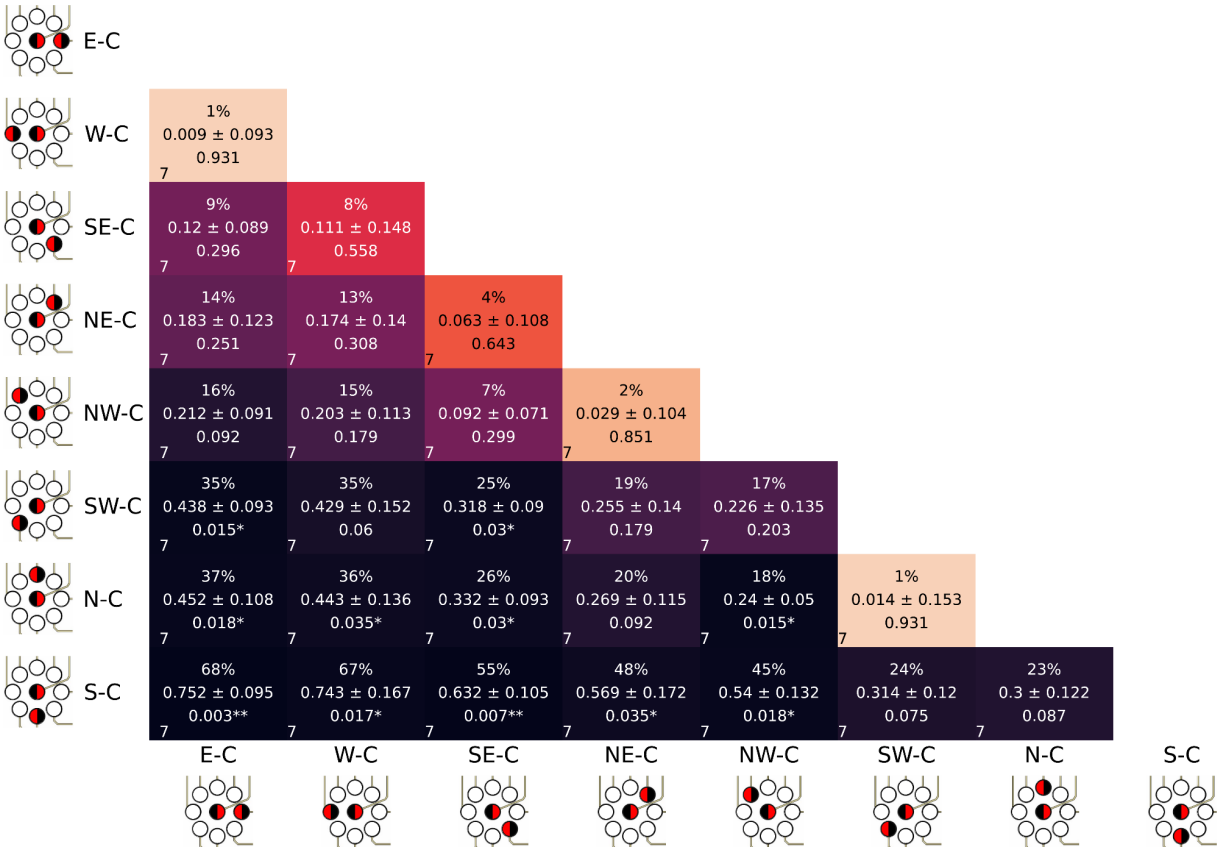

Figure S8. Pairwise efficacy comparison of radial bipolar configurations on the circular array. The south-center (S-C) configuration is most effective, followed by north-center (N-C). Each cell reports the threshold increase of the configuration in the column relative to the row, with darker cell color indicating lower p-value, after correcting for false discovery rate across all pairwise comparisons. Cells display: (top) percentage increase in threshold of the column relative to the row, (middle) mean threshold difference ± SEM on the $\log_2$ scale, (bottom) corrected p-value, and (bottom left) degrees of freedom for the paired t-test. Rows are ordered based on the number of other configurations each beat in head-to-head comparisons, with more effective configurations at the bottom.

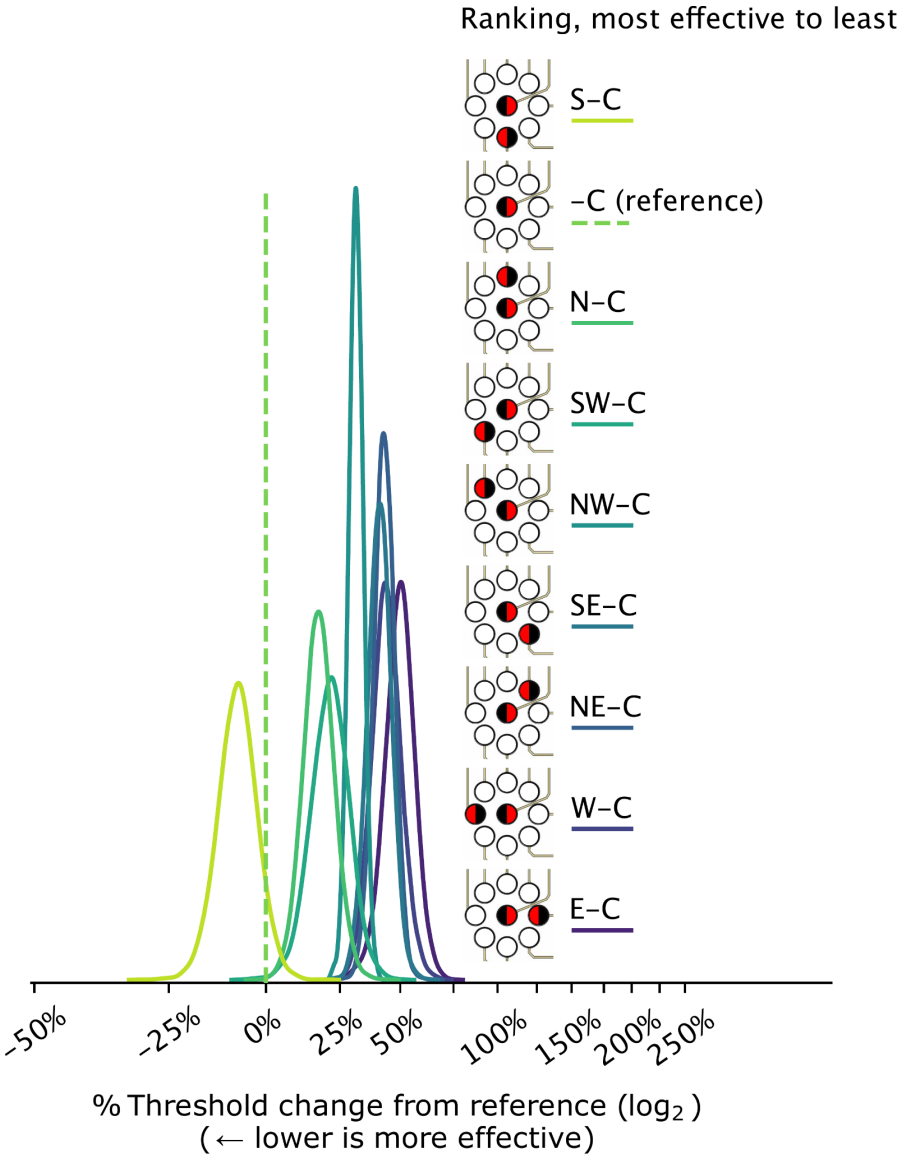

Figure S9. Bayesian comparison of radial bipolar configurations on the circular array. Posterior distributions summarize change in threshold relative to the center (C) contact. The south-center (S–C) configuration yields lower thresholds than C with probability 0.94, and lower thresholds than all radial bipolar configurations with probability 1.00.

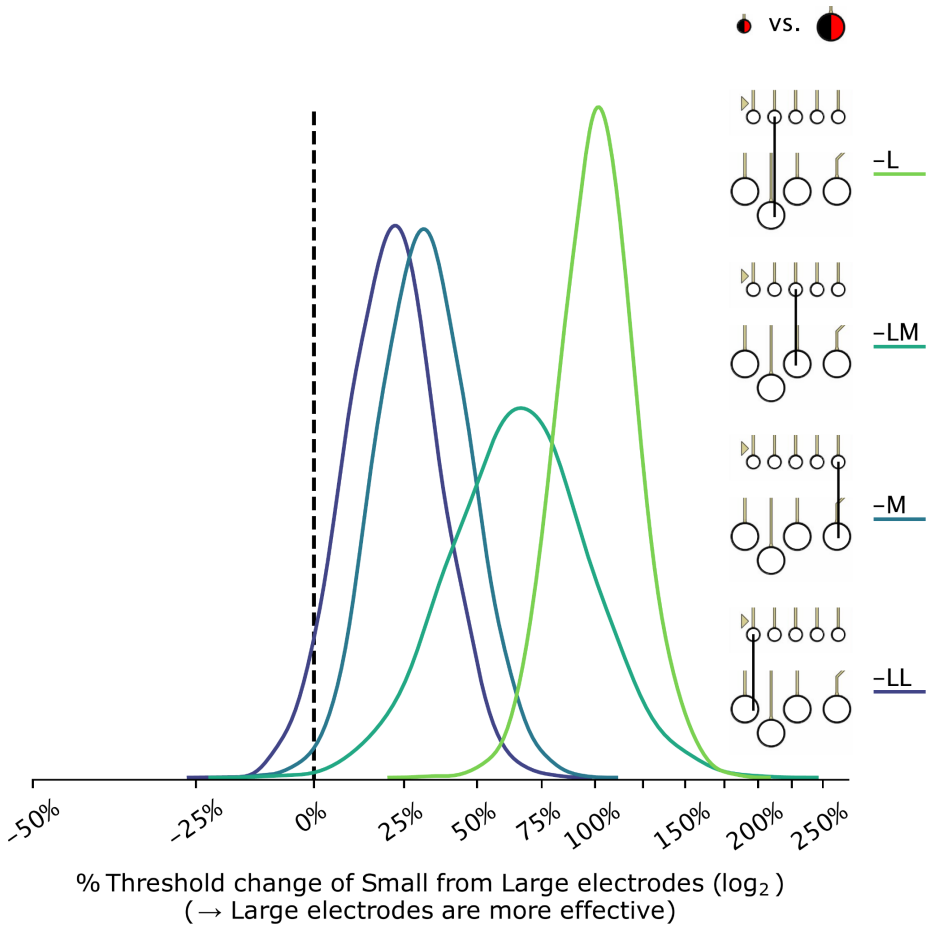

Figure S10. Bayesian comparison of large and small contacts at similar mediolateral positions. Posterior distributions summarize the threshold change of small relative to large electrodes, where positive values indicate greater efficacy of large contacts. Large electrodes are more effective at all positions, as shown by distributions shifted to the right of zero, with high posterior probabilities: 1.00 at L and LM, 0.99 at M, and 0.95 at LL.

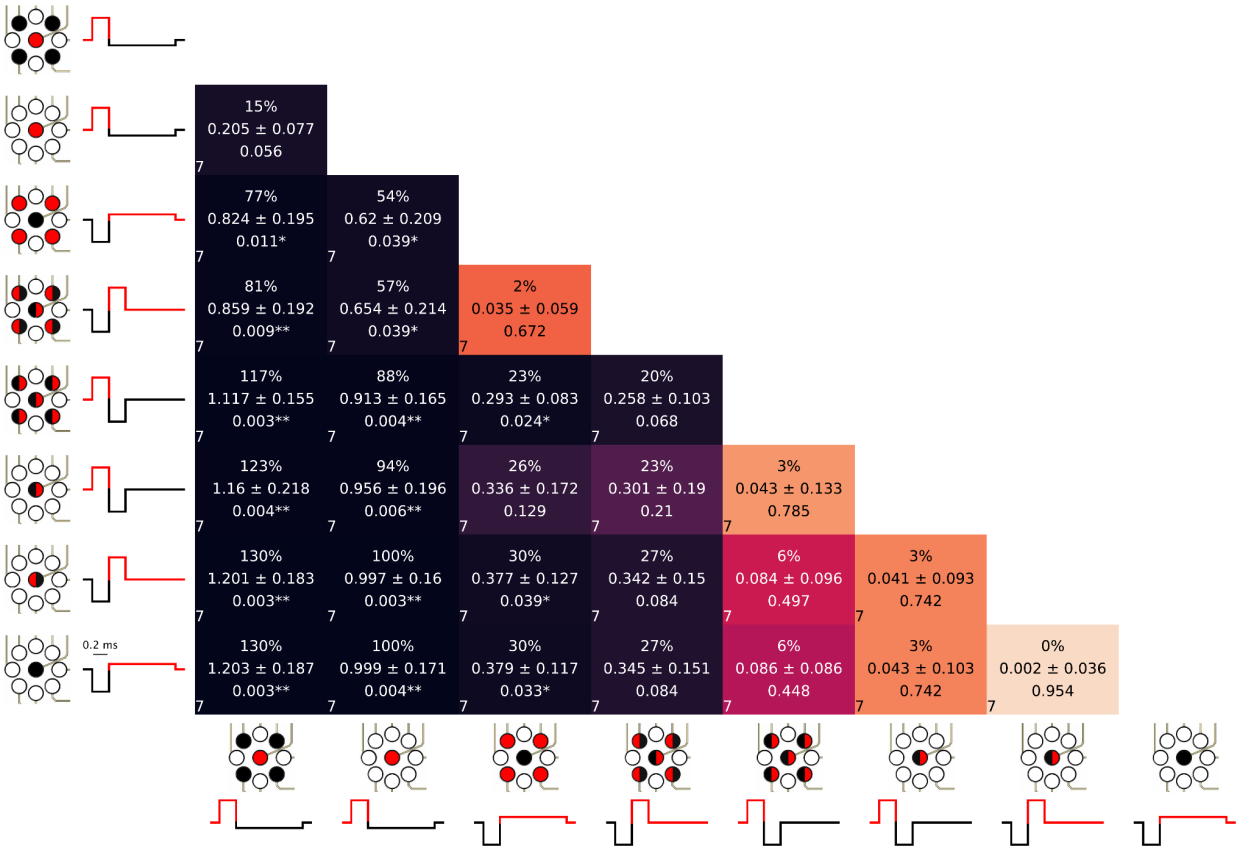

Figure S11. Pairwise efficacy comparison of configurations tested with biphasic and pseudomonophasic pulses on the circular array. Cells display: (top) percentage increase in threshold of the column relative to the row, (middle) mean threshold difference ± SEM on the $\log_2$ scale, (bottom) corrected p-value, and (bottom left) degrees of freedom for the paired t-test. Rows are ordered based on the number of other configurations each beat in head-to-head comparisons, with more effective configurations at the bottom.

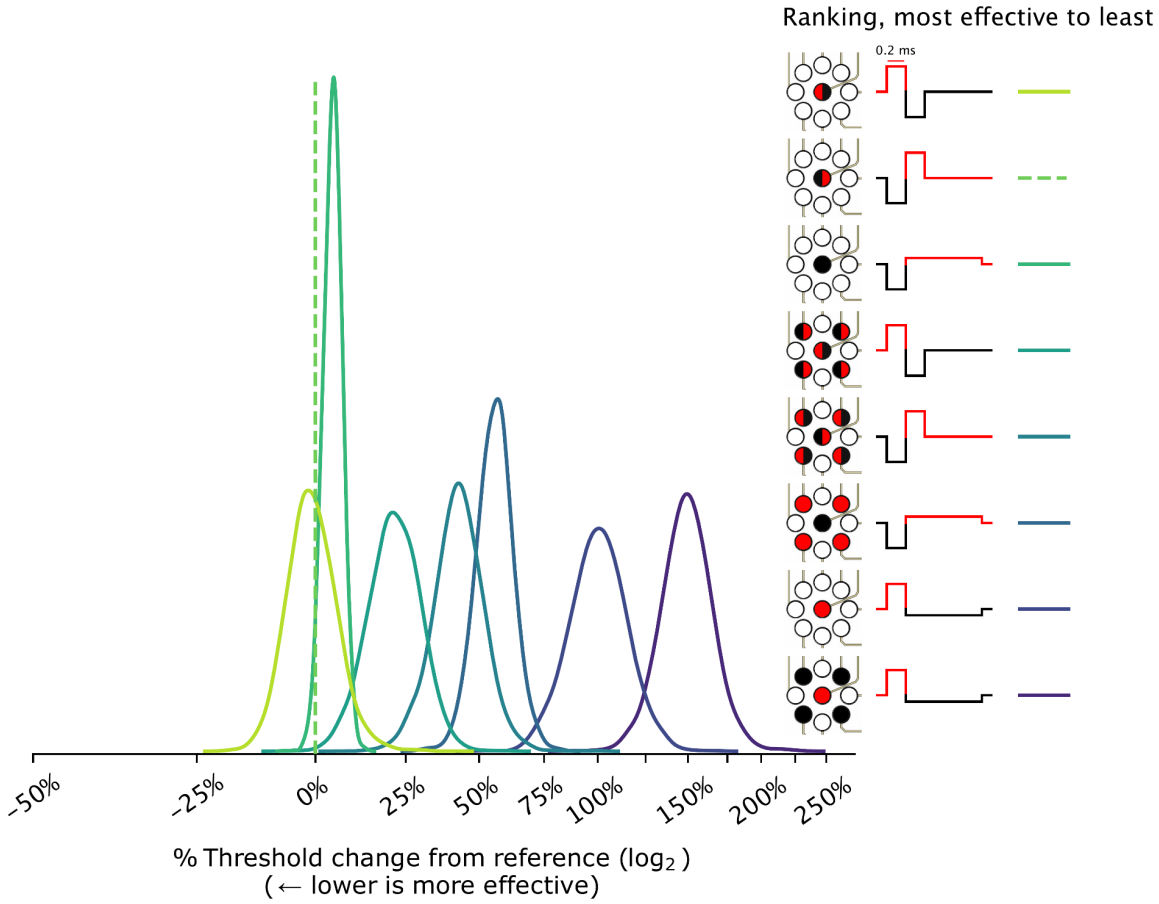

Figure S12. Bayesian comparison of configurations tested with biphasic and pseudomonophasic pulses on the circular array. Posterior distributions summarize threshold changes relative to biphasic stimulation with a cathode at the center (C) contact and a distant return. With a distant return, biphasic stimulation with either a cathode or anode at the center, and pseudomonophasic stimulation with a center cathode have comparable efficacy and outperform other configurations with high posterior probabilities, as indicated by low overlap in their distributions.

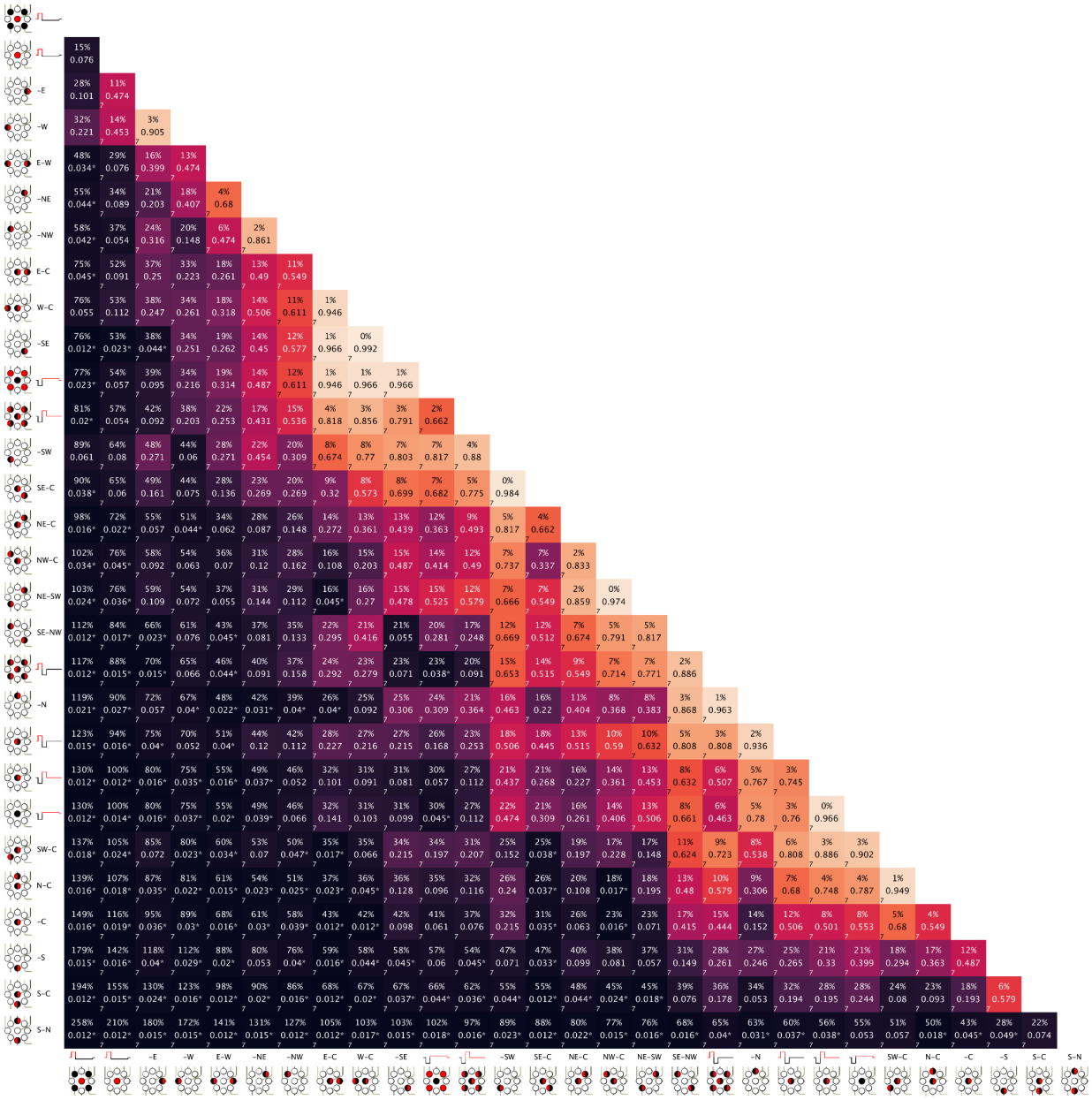

Figure S13. Pairwise efficacy comparison of all configurations tested from the circular array. While the S-N and S-C configurations are not significantly different ($p = 0.074$), the S-N configuration is significantly more effective ($p < 0.05$) than all other tested configurations. Each cell reports the threshold increase of the position in the column relative to the row, with darker cell color indicating lower p-value, after correcting for false discovery rate across all pairwise comparisons. Cells display: (top) percentage increase in threshold of the column relative to the row, (bottom) corrected p-value, and (bottom left) degrees of freedom for the paired t-test. Rows are ordered based on the number of other positions each beat in head-to-head comparisons, with more effective positions at the bottom. Stimulation configurations marked with waveform icons were tested in the same experiment, and those marked with cardinal directions were tested in a separate, time-adjacent experiment.